Quantifying numerical mixing in a tidally forced global eddy-permitting ocean model

Alex Megann

National Oceanography Centre, Empress Dock, Southampton SO14 3ZH, UK

Abstract

An ensemble of experiments based on a ¼° global NEMO configuration is presented, including tidally forced and non-tidal simulations, and using both the default z* geopotential vertical coordinate and the z~ filtered Arbitrary Lagrangian-Eulerian coordinate, the latter being known to reduce numerical mixing. This is used to investigate the sensitivity of numerical mixing, and the resulting model drifts and biases, to both tidal forcing and the choice of vertical coordinate. The model is found to simulate an acceptably realistic external tide, and the first-mode internal tide has a spatial distribution consistent with estimates from observations and high-resolution tidal models, with vertical velocities in the internal tide of over 50 meters per day. Tidal forcing with the z* coordinate increases numerical mixing in the upper ocean between 30°S and 30°N where strong internal tides occur, while the z~ coordinate substantially reduces numerical mixing and biases in tidal simulations to levels below those in the z* non-tidal control. The implications for the next generation of climate models are discussed.

Plain Language Summary

Oceanic tides are known to cause a large fraction of the mixing in the ocean interior. In numerical ocean models additional spurious mixing arises from errors in the advection of temperature and salinity. This means that the internal tide, with vertical velocities that can exceed 50 meters per day, can cause significant amounts of this numerical mixing. We show that adding tidal forcing to a global ocean model with ¼° horizontal resolution (about 25 km at the Equator) causes significant numerical mixing in the upper ocean between 30°S and 30°N, where strong internal tides are present. We show in addition that changing the vertical coordinate of the model from the standard fixed-depth coordinate to one ("z-tilde") in which the grid is allowed to move vertically with the internal tide substantially reduces the spurious mixing, and in fact the model with z-tilde and tides has lower temperature biases relative to observed values than the standard model without tides.

Key points

1. Tidal forcing is applied to a global ¼-degree ocean model and the external and internal tides are acceptably realistically simulated.
2. With the default z* vertical coordinate, significant numerical mixing occurs in regions of strong internal tide.
3. With the z~ ALE coordinate numerical mixing and temperature biases are substantially reduced to levels below those in the non-tidal control.

1. Introduction

The contribution of turbulent mixing from internal tides to the total mixing in the ocean is estimated to be about 30% of the total dissipation (Egbert and Ray, 2001). It is the dominant mechanism by which Antarctic Bottom Water is mixed with the overlying deep waters (Hogg et al.; 1982; Munk and Wunsch, 1998; St Laurent and Garrett, 2002; De Lavergne et al., 2016), thereby providing a balance over the long term to the production of bottom waters around Antarctica. Mixing from internal tides is also believed to be significant elsewhere, including playing a major role in supporting the meridional overturning circulation (Webb and Suginohara, 2001; Wunsch and Ferrari, 2004). Nevertheless, few global ocean models, particularly those with the horizontal resolution of between 0.25° and 1° that is currently typical of climate models, have historically included tidal forcing. The main reason for this is that such models either fail to represent the internal tide at all, or can resolve at most the first internal mode: the wavelength of a mode-1 internal tide with period 12 hours is between 50 and 90 km, and that of the second mode typically between 40 and 55km (e.g. Zhao, 2018). This means that these models are far from being able to simulate the energy cascade of internal waves down to wavelengths of a few hundred meters and high vertical modes (Garrett and Munk, 1975; Sakai et al., 2021), at which point they break and mixing occurs (Vic et al., 2019).As a result, internal tidal motions in these models cannot contribute significant levels of mixing through this mechanism.

Although ocean general circulation models (OGCMs) with tidal forcing do not explicitly represent the small-scale mixing that results from the energy cascade from internal tides, substantial advances have been made over the last two decades in simulating tides in OGCMs with realistic domains and surface forcing (see Arbic, 2022 for a comprehensive overview). Arbic et al. (2010) showed that a 1/12.5° global HYCOM model with realistic bathymetry and surface forcing represented the barotropic tide well, and that the internal tides were similar in both their spatial patterns and their amplitudes to those derived from satellite altimetry, even though only low internal modes were present. Several studies have found that adding tidal forcing to models tends overall to increase the realism of the models. The presence of tidal motions appears to give particular benefit in polar regions, where interactions between tides and sea ice contribute processes absent from non-tidal simulations. Holloway and Proshutinsky (2007) compared tidally forced and non-tidal models of the Arctic Ocean, summarizing that tidal-induced mixing in the Arctic Ocean plays an important role in the global conveyer belt. Luneva et al (2015) investigated the influence of tidal forcing in a ¼° model of the Arctic, finding that the tidal motions caused significantly increased (and more realistic) levels of mixing, in particular between the cold halocline layer and the warm Atlantic Water layer, which was associated with enhanced melting of sea ice. Jourdain et al. (2019) reached a similar conclusion from a regional simulation of the Amundsen Sea with and without tidal forcing.

Improvements in fidelity resulting from the inclusion of tidal forcing in OGCMs have also been found outside ice-covered regions. Song et al. (2023) compared global implementations of the Finite-volumE Sea ice–Ocean Model (FESOM2.1) with and without explicit tidal forcing, concluding that tides strengthened both the upper and lower cells of the global overturning circulation, as well as the Antarctic Circumpolar Current (ACC). Katavouta et al. (2022) reported a marked improvement in the representation of critical water masses in a regional 1/12° model of the Indonesian

Archipelago when tides were present. Mixing from the barotropic tide has been hypothesized to be critical for realistic distributions of biogeochemical tracers on shelves (Sharples et al., 2007), as well as over mid-ocean ridges (Tuerena et al., 2019).

Since models with eddy-permitting resolution are unable to represent the full internal tide spectrum, and hence omit the significant levels of mixing from this source, the mixing effect of tides is often provided by a parameterization scheme. Following the pioneering work of St Laurent et al. (2002), practical implementations include those of Simmons et al. (2004), Jayne (2009), Saenko and Merryfield (2005) and of de Lavergne et al. (2020). Such schemes typically augment the vertical global mixing based on the large-scale stratification with locally enhanced mixing, based on the effect of rough bottom topography on stratified tidal flows that are derived from an external barotropic tidal model. The earlier approaches evaluate a spatially varying energy dissipation rate, according to local turbulent energy levels derived from the tidal velocity field, while that of de Lavergne et al. (2020) adds a representation of the effects of remotely generated internal tides.

A known weakness of models based on geopotential vertical coordinates is that the large vertical velocities that characterize internal waves and tides, which can exceed 50 meters per day, cause vertical advection of tracers, and the numerical advection scheme has a small irreversible, or diffusive, component (Griffies et al, 2000) which leads to unphysical numerical tracer mixing. The default vertical coordinate in version 4 of the Nucleus for European Marine modelling of the Ocean (NEMO v4.0, Madec et al, 2019) is the nonlinear free surface or Variable Volume Layer (VVL) scheme (Adcroft and Campin, 2004; Levier et al, 2007), usually referred to in shorthand as z*, which represents external gravity waves as changes to the layer vertical scale, scaled uniformly over the water column with the surface height anomaly. Megann (2018) evaluated an effective diapycnal diffusivity based on density transformation in a global ¼° NEMO and found that over much of the ocean interior this was between five and ten times as large as the diffusivity calculated in the TKE mixing scheme of the model. The z~ vertical coordinate (Leclair and Madec, 2011) is intended to reduce this contribution to numerical mixing by replacing Eulerian vertical velocities relative to a fixed grid from tides and internal gravity waves by displacements of the grid on timescales shorter than a few days, reverting to the z* grid on longer timescales. Megann et al. (2022), henceforth referred to as MCS2022, used an ensemble of global 1/4° NEMO simulations with z* and z~ with a range of timescale parameters to demonstrate that z~ performs as intended, transforming Eulerian advective vertical velocities associated with internal waves into near-adiabatic displacements of the vertical coordinate. In this configuration z~ was shown to give almost unequivocal improvements to model performance, reducing a diagnosed effective diapycnal diffusivity by at least 10% and consistently reducing drifts in the temperature and salinity at all depths. Lengthening the filter timescale parameter from the default of 5 days up to 40 days was found to robustly strengthen the benefits of z~, after which point diminishing returns started to set in. Until now, the effectiveness of the z~ coordinate has not been assessed in a realistic simulation with tidal forcing, but since the 12-hour and 24-hour periods of tidal forcing are well within the time scales addressed by z~, we expect it to confer similar advantages as those already demonstrated in the presence of internal waves.

This paper forms a companion to MCS2022, using the same ocean configuration and extending the ensemble developed under that study to include tidal forcing. The questions we shall address in this paper are:

1) How well does the model simulate external and internal tides with z* and z~, taking the limited resolution into account?

2) Does the z~ vertical coordinate work as designed in a tidally forced global configuration?

3) What is the sensitivity of numerical mixing to tidal forcing?

4) How much does z~ reduce numerical mixing from internal waves and tides?

5) How do tides and z~ affect model drifts and biases?

In Section 2 we describe the model and introduce the experimental design. In Section 3 we assess the representation of the external and internal tides in the simulations and perform first-order checks on the functioning of z~ in a model configuration with tidal forcing. In Section 4 we quantify the mixing in the simulations, and in Section 5 we investigate the effect of tides and z~ separately and in combination on the model fields and large-scale circulation. Finally, Section 6 is a Summary and Discussion.

2. Model description and experimental design

2.1 Model description

The GO8p0.1 model configuration used in this study is identical to that described in MCS2022, so we will include only a brief description here. It is based on the GO6/GO7 ocean configurations (Storkey et al, 2018), but is built on version 4.0 of the Nucleus for European Marine Modelling ocean model (NEMO v4.0, Madec et al, 2019), whose default sea ice component is the Sea Ice modelling Integrated Initiative model (SI^3), whereas the earlier configurations used version 3.6-stable of NEMO and the CICE sea ice model. The grid is the eORCA025 extended global 1/4° resolution grid (Barnier et al, 2006), which is a quasi-isotropic bipolar grid with poles at land points in Siberia and Canada, a southward grid extension to allow simulation of the Antarctic ice shelves, and a Mercator projection grid elsewhere. We note that the Arctic regional model used by Luneva et al, (2015) is an exact subdomain of the grid used in the present model, although those authors used a hybrid terrain-following vertical coordinate, in contrast to the fixed z* vertical coordinate used here.

Horizontal viscosity is bilaplacian with the default value of A_{Lm} =-1.5 $x10^{11}$ m^4s^{-1} at the Equator, with values reduced polewards as the cube of the maximum grid cell dimension to avoid instability in the momentum diffusion equation (see Griffies, 2004). Tracer advection is second-order Flux Corrected Transport (FCT), also known as Total Variance Dissipation (TVD; Zalesak, 1979), for both horizontal and vertical advection of tracers. Lateral diffusion of tracers is along isoneutral surfaces, with a coefficient of 150 m^2s^{-1}; the default in NEMO v4 is the scheme of Redi (1982), as implemented by Cox (1987). A mesoscale eddy parameterization scheme is not used. The vertical mixing scheme is a modified version of the Turbulent Kinetic Energy (TKE) scheme (Gaspar et al, 1990; Madec, 2008), with a background vertical eddy diffusivity of 1.2×10^{-5} m^2 s^{-1}, which decreases linearly with latitude from 15°N and 15°S towards

a value of 1.2×10^{-6} m^2 s^{-1} between 5°N and 5°S.

The ocean is initialized at rest from a 1995-2004 average of the EN4 climatology (Good et al., 2013), and integrated from 1976 to 2005, forced with CORE2 interannual fields (Large and Yeager, 2009), with the last ten years used for the principal analysis. The forcing frequencies were as follows: 6-hourly wind speed, air temperature and humidity; daily longwave and shortwave radiation, with a diurnal cycle applied to the latter; and monthly mean precipitation.

2.2 The z~ vertical coordinate

Three of the experiments described here use the default z* vertical coordinate, which, as noted in the Introduction, has been shown to produce spurious diapycnal mixing of tracers in the presence of internal waves, and we shall also present results from experiments with the z~ vertical coordinate. The implementation of this in NEMO v4.0 is identical to that described in MCS2022; Appendix A1 of that paper includes a full description of the operation of z~ as presented by Leclair and Madec (2011), and Appendix A2 describes the modifications applied to the code that are needed to ensure stable operation in a global domain with realistic bathymetry and coastlines. These include checks on negative thicknesses; strong restoration to z* near the sea bottom; reversion to z* in water shallower than 100m; and extra thickness smoothing.

The z~ scheme in NEMO includes two timescale parameters: $\tau_{\sim}$ is the filter timescale for frequency division between the quasi-isopycnal regime at high frequencies and the z* regime at low frequencies, and τ_z is the timescale for restoration of the interface depths to z*. We select two pairs of values for these from the z~ ensemble described by MCS2022: the default settings of $\tau_{\sim}$=5 days and τ_z=30 days; and $\tau_{\sim}$=20 days and τ_z=60 days, the latter combination being found to give a marked enhancement, with respect to the default settings, of the effectiveness of z~ in reducing numerical mixing from internal waves at close to the inertial period.

2.3 Tidal forcing

Tidal forcing is applied in NEMO as an additional barotropic force in the momentum equation (see Madec et al., 2019 for details) and in the present application includes five tidal harmonics: the semidiurnal components M2, S2 and N2; and the diurnal components K1 and O1. The scalar approximation for self-attraction and loading (Accad & Pekeris, 1978), was applied. Log-layer bottom drag was enabled. with a base drag coefficient of 1.0×10^{-3}. It was found that tidal forcing with the standard eORCA025 bathymetry, using a default minimum depth of 9.8 meters (level 8), gave fatal errors at runtime, with unacceptably high velocities, so this was increased to 16.5 meters (level 11) for the tidally forced configurations.

Because the internal tide was not expected to be well resolved at the ¼° resolution, and therefore was therefore unlikely to provide realistic levels of tidal mixing, a code modification was used (see Appendix A for details of the model sources) that applies the tidal mixing parameterization of Simmons et al (2004), with modifications in the Indonesian throughflow region (Koch-Larrouy et al., 2008), to all the non-tidal experiments and all except one of the tidally forced experiments. We shall show that this scheme enhances the explicit diffusivity in the mixing scheme in the ocean interior over major bathymetric features.

2.4 Experimental strategy

The main aims of this study are twofold: firstly, to investigate the effects of tidal forcing on numerical mixing in a 1/4° global NEMO configuration; and secondly, to evaluate the benefits of the z~ vertical coordinate in ameliorating the numerical mixing from the internal tide. To this end, we implement a six-member "main" ensemble consisting of three pairs of experiments, one of each pair tidally forced and the other not tidally forced; the first pair uses the z* vertical coordinate; the second uses z~ with the default timescale parameters of $\tau_{\sim}$=5 days and τ_z=30 days; and the third pair uses z~ with the timescale parameters extended to $\tau_{\sim}$=20 days and τ_z=60 days.

Two additional z* simulations are included. One experiment *zstar_notide_16m* does not apply tidal forcing, but uses the modified bathymetry used for the tidally forced experiments (i.e. a deeper minimum shelf depth); this is added to isolate any potential sensitivities of the metrics to the changed minimum shelf depth. The second, *zstar_tide_nomix,* has tidal forcing applied but the Simmons et al (2004) tidal mixing parameterization is not enabled; this serves to illustrate the limited ability of the existing TKE mixing scheme to represent the mixing effect of tides. Table 1 summarizes the experiments in the ensemble; we shall principally discuss the six "main" experiments, only adding the two additional experiments to line plots of global fields. We note that *zstar_notide, ztilde_5_notide* and *ztilde_20_notide* are the same simulations as those referred to as *zstar*, *ztilde_5_30* and *ztilde_20_60*, respectively, in MCS2022.

Run	**Vertical coord.**	**Z~ time scales**	**Tidal forcing**	**Tidal mixing param^{n}**	**Min shelf depth**
zstar_notide	z*	-	N	Y	9.8 m
ztilde_5_notide	z~	5/30 days	N	Y	9.8 m
ztilde_20_notide	z~	20/60 days	N	Y	9.8 m
zstar_tide	z*	-	Y	Y	16.5 m
ztilde_5_tide	z~	5/30 days	Y	Y	16.5 m
ztilde_20_tide	z~	20/60 days	Y	Y	16.5 m
zstar_notide_16m	z*	-	N	Y	16.5 m
zstar_tide_nomix	z*	-	Y	N	16.5 m

Table 1: Model integrations.

3 Assessment of the simulated external and internal tide

In this section we assess the external (barotropic) and internal (baroclinic) tides in the three main tidally forced simulations against both other general circulation models and high-resolution tidal models. Our objectives here are: to demonstrate firstly that the model is capable of simulating an acceptably realistic external tide; to show that internal tides are reproduced with realistic spatial distributions and with amplitudes that are sufficient to test the z~ coordinate; and finally that implementing z~ does not have a significant effect on the internal tide field.

3.1 Representation of the barotropic tide

The harmonics of the barotropic tide were evaluated for each integration from hourly sea surface elevation over the first three months of 1996, and we validate them here against the respective harmonics from the FES2014 global ocean tide atlas (Lyard et al, 2021). Figure 1 shows the amplitudes and phases for the FES2014 harmonics (top panels) and those from the *zstar_tide* simulation (bottom panels). The amplitudes of the M2 and S2 semidiurnal tides in *zstar_tide* (Figures 1(a) and (b)) are 10-30% larger than in FES2014, while that of N2 (Figure 1(c)) is a little smaller, although the locations of the largest tides in all the harmonics in the simulation are generally close to those in the reference, as are the amphidromes (locations of zero amplitude). The diurnal tides K1 and O1 (Figures 1(d) and (e)) are again comparable in both amplitude and phase to the reference.

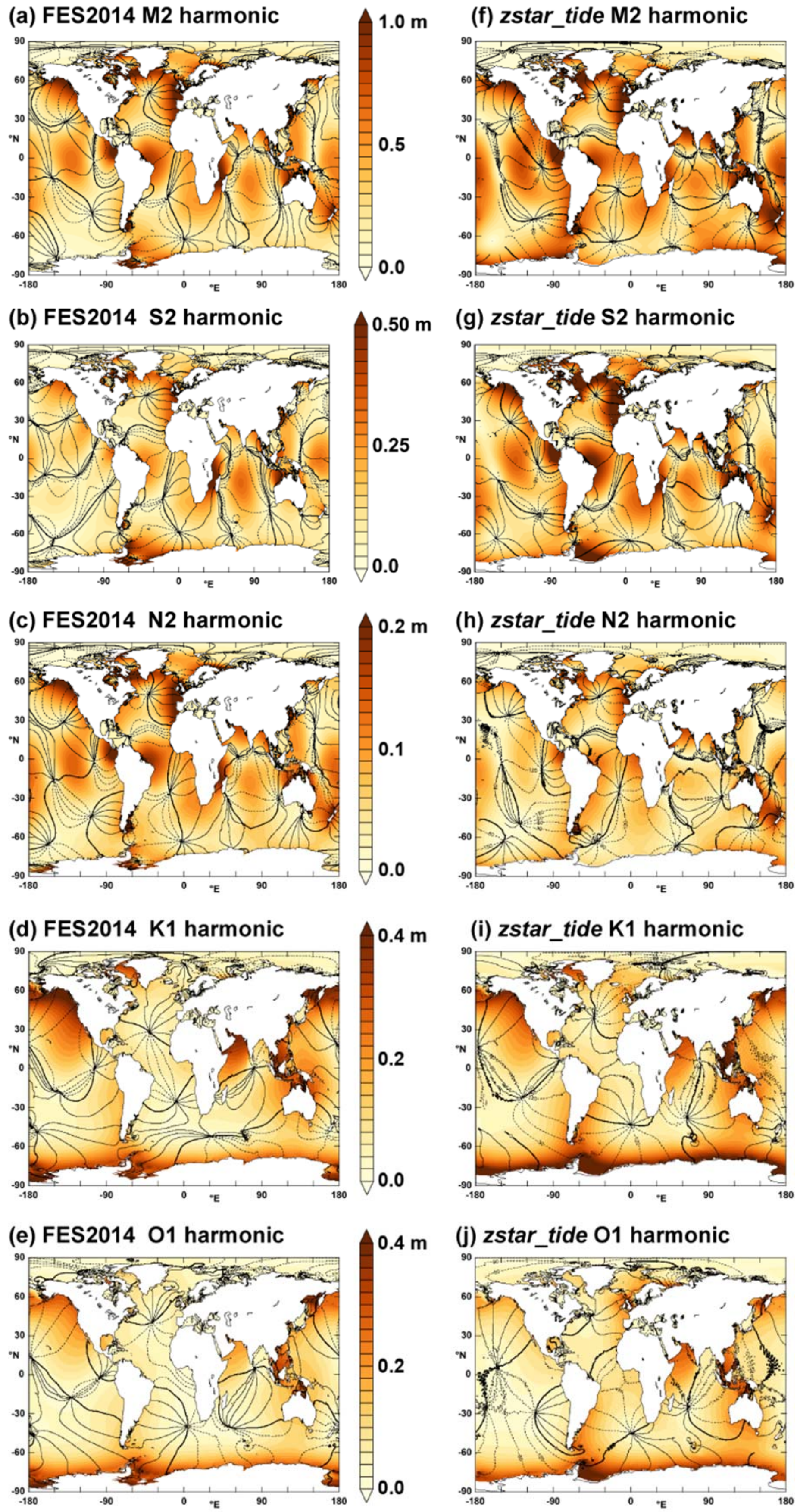

(a) FES2014 M2 harmonic
(b) FES2014 S2 harmonic
(c) FES2014 N2 harmonic
(d) FES2014 K1 harmonic
(e) FES2014 O1 harmonic
(f) zstar_tide M2 harmonic
(g) zstar_tide S2 harmonic
(h) zstar_tide N2 harmonic
(i) zstar_tide K1 harmonic
(j) zstar_tide O1 harmonic
1.0 m
0.5
0.0
0.50 m
0.25
0.0
0.2 m
0.1
0.0
0.4 m
0.2
0.0
0.4 m
0.2
0.0
°N
°E

Figure 1. Tidal harmonic amplitudes of surface elevation in meters: (a) M2; (b) S2; (c) N2; (d) K1; and (e) O1 from the FES2014 dataset; and (f) M2; (g) S2; (h) N2; (i) K1; and (j) O1 from the *zstar_tide* simulation. The black contours show the phase of each harmonic, with dashed lines representing a negative sign of the phase.

3.2 Representation of the internal tide

With a fixed vertical coordinate, it is straightforward to discuss the internal tide in terms of the vertical velocity with respect to the fixed coordinate surface; we could also in principle validate this field against measurements of the vertical velocity from moored arrays. In the case of the z~ coordinate, however, it is not appropriate to define the internal tide in terms of vertical velocities with respect to the model grid, so we use the method introduced by Ray and Mitchum (1997), which has been applied to satellite altimeter data by Ray and Zaron (2016), Zhao et al. (2016) and others, and to the simulated surface elevation in a global 1/12° model by Arbic et al. (2012), to derive a representation of the internal tides that will enable us to characterize the sensitivity of the internal tide consistently for all the tidally forced experiments. This involves projecting the sea surface height onto each of the harmonic frequencies, and for each component applying a low-pass spatial filter to isolate the large-scale external component (the effect on the sea-surface height) of the internal tidal signal. The low-pass filtered signal is then subtracted from the original harmonic, and most of the residual signal in the surface height will therefore be associated with the internal tide. In this case we use a Hanning smoother with width 9 grid cells.

Figure 2 shows the surface signature of the M2 semidiurnal and the K1 diurnal internal tides, evaluated as above. The panels for M2 can be compared directly with Figure 4(a) of Zhao et al. (2016), which shows the global M2 surface tide derived from satellite altimetry: the spatial structure of the regions of high amplitude in the simulations correspond well to those in the observational estimate, although the amplitude of the simulated internal tide is less than half that in the altimetry data in the Pacific, and still weaker in the Atlantic. We also compare Figures 2(a)-(c) with Figure 8 of Arbic (2022), which shows the M2 component of the SSH variability around the Hawaiian Archipelago in a range of tidal models along with the 1/12° tidally forced simulation of the Hybrid Coordinate Ocean Model (HYCOM, Bleck

2002): the amplitude of the M2 component in the present model is between 30 and 50% of that in the 1/12° simulation, but comparable with that in several of the other tidal models with a similar resolution to that of the present configuration. This reduction in internal tide energy in the present ¼° configuration is not altogether surprising, since the first baroclinic mode of the semidiurnal tide typically has a wavelength of between 50 and 90 km (e.g. Zhao, 2018), so is only marginally resolved in most locations at the 1/4° resolution of the eORCA025 grid. Examination of the vertical structure of the vertical velocity in *zstar_tide* (see Figure 4(d), for example) confirms that the internal tide in this configuration is present almost exclusively in the first baroclinic mode.

It is of note that the largest amplitudes of the internal tides – even of the semidiurnal components - are found mainly between 30°S and 30°N, and especially in the Pacific, where energetic sources of internal tides include the Izu-Ogasawara-Marianas Ridge south of Japan, the Solomon Archipelago east of Papua New Guinea, the Hawaiian Ridge, and the Tuamoto Archipelago south of the Equator.

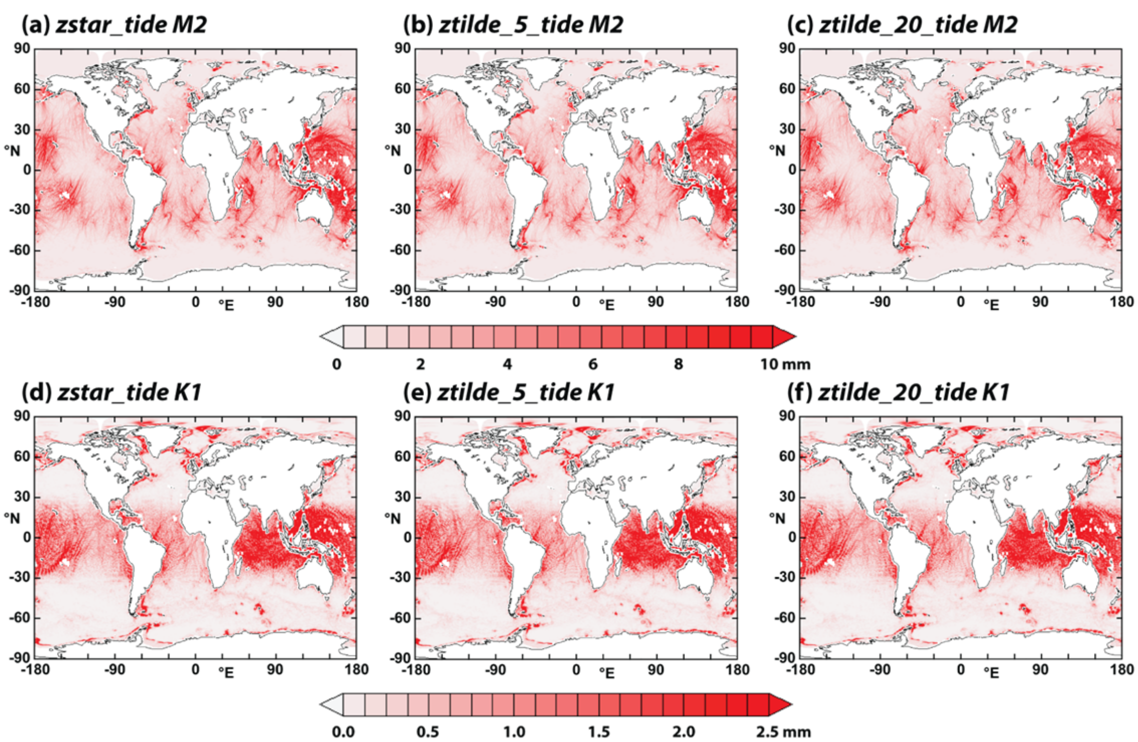

Figure 2. The surface signature of the internal tide, calculated using the method of Arbic (2012): the M2 harmonic in (a) *zstar_tide*; (b) *ztilde_5_tide*; and (c)

ztilde_20_tide; and that of the K1 internal tide in (d) *zstar_tide*; (e) *ztilde_5_tide*; and (f) *ztilde_20_tide*.

The SSH projection of the internal tide is found to be only weakly sensitive to the choice of vertical coordinate. Table 2 lists the RMS value of the surface elevation projected onto the five tidal harmonics for each of the tidally forced simulations, along with the difference in global RMS signal between *ztilde_20_tide* and *zstar_tide*. The RMS value in *ztilde_20_tide* is not consistently larger or smaller than in *zstar_tide*, and the fractional differences with z~ in the M2 and S2 semidiurnal tides are of order 10^{-3}, which we do not consider significant.

Harmonic	***zstar_tide* RMS (mm)**	***ztilde_5_tide* RMS (mm)**	***ztilde_20_tide* RMS (mm)**	***ztilde_20_tide* minus *zstar_tide***
M2	5.445	5.440	5.449	0.004
S2	2.565	2.559	2.562	-0.003
N2	0.842	0.835	0.821	-0.021
K1	1.505	1.510	1.519	0.014
O1	1.166	1.174	1.175	0.009

Table 2: The global RMS amplitude (in mm) of the surface elevation projection of each of the interior tide harmonics in the three tidally forced simulations, and the difference between the RMS amplitude between *ztilde_20_tide* and *zstar_tide*.

3.3 Transformation of Eulerian tidal velocities by the z~ coordinate

MCS2022 demonstrated the effectiveness of z~ in converting vertical velocities relative to the fixed z* coordinate grid (which we refer to as Eulerian vertical velocities), on timescales typical of internal waves into displacements of the grid. Using as a case study a water column in the subtropical North Atlantic where energetic Near-Inertial Gravity Waves (NIGWs) occur, a reduction in the Eulerian vertical velocity, with respect to that in the z* control, of a factor of 4 with the default z~ timescale parameters and a factor of 25 with the longest timescales was observed. Since the semidiurnal and diurnal tides have periods comparable to those of near-inertial gravity waves (the latter have periods between 15 and 24 hours in the latitude range 30-50°N), we expect this coordinate to be equally effective, with a given selection of timescale parameters, in its response to internal tides as it is with NIGWs.

Figure 3 shows the hourly Eulerian vertical velocity on level 55 (a nominal depth of 2021 m) in the Pacific at the start of year 1996 of each of the six main experiments. In the non-tidally forced experiments (top panels), the NIGWs, which in z* (Figure 3(a)) are characterized by near-plane wave fronts with vertical velocities of up to 50 meters per day, are almost entirely converted in the z~ experiments (Figure 3(b) and (c)) to vertical coordinate displacements, particularly with the longer z~ timescale (Figure 3(c)). Equatorial waves, which were identified in a related NEMO simulation at the same resolution (Blaker et al., 2021), are visible within 8-10° of the Equator; since these have periods of between 2 and 8 days, the Eulerian velocities associated with these are only partially transformed into coordinate displacements, relative to the NIGWs and internal tides, with a 5-day filter timescale (Figure 3(b)), but are substantially reduced in the case of the 20-day filter timescale (Figure 3(c)).

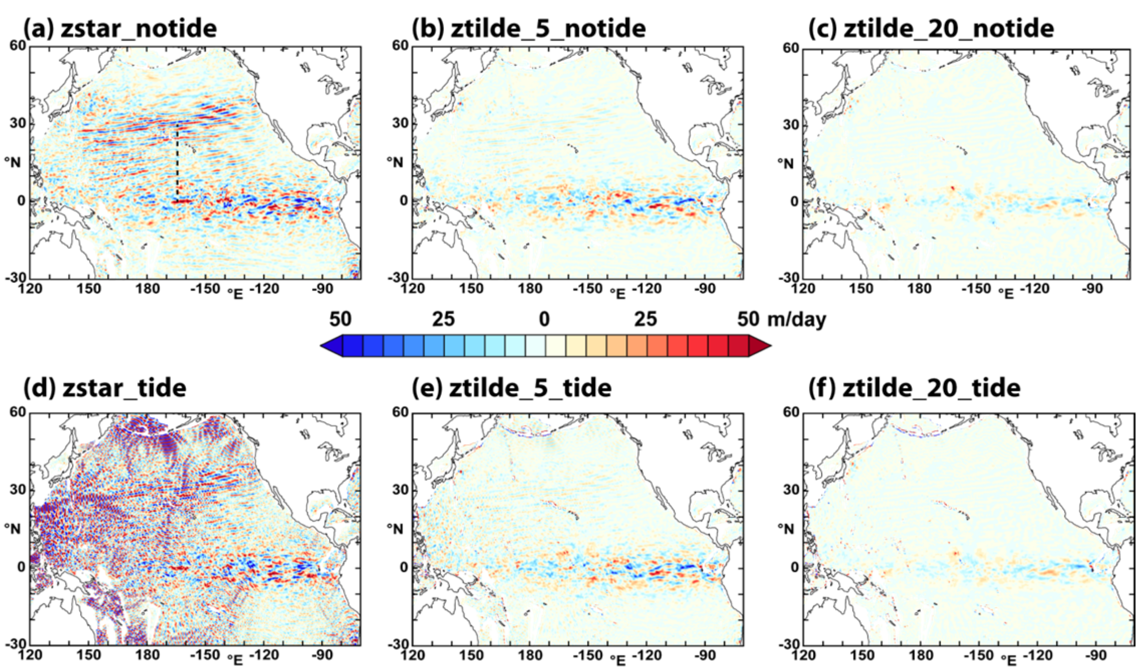

Figure 3. Hourly Eulerian vertical velocities in the Pacific at nominal 2,000m depth in (a) *zstar_notide*; (b) *ztilde_5_notide*; (c) *ztilde_20_notide*; (d) *zstar_tide*; (e)

ztilde_5_tide; and (f) *ztilde_20_tide*. The dashed black line in panel (a) indicates the position of the sections that will be plotted in Figure 4.

When tidal forcing is introduced with z*, the internal tides can be seen to dominate the internal wave field over much of the Pacific (Figure 3(d)). Internal tide trains with amplitudes greater than 50 meters per day are found almost everywhere in the basin west of about 130°W, radiating from the shelf edges and island chains. The directions and relative intensities of the tidal rays in this panel may be matched to many of those in the surface signatures of the internal tides (Figure 2(a)): particularly strong internal tide fields are visible in both figures in the regions west of 180°E and around the Hawaiian Archipelago. A prominent exception to this is the large amplitude of the vertical oscillations associated with internal tides generated close to the Aleutian Archipelago (see Figure 3(d)), which do not have a strong surface signature in Figure 2(a). Enabling z~ with tidal forcing (Figures 3(e) and (f)) has a comparable effect as in the non-tidal simulations, and the signature of the internal tides in the Eulerian vertical velocities, as with that of the NIGWs, is reduced by at least a factor of ten. Comparing the equatorial waves between the top and bottom rows of panels in Figure 3 confirms that they are unaffected to first order by the presence of tides; this is to be expected, since, as shown by Blaker et al., 2021, these are to first order deterministic, being locally forced by the wind stress.

Figure 4 shows the vertical structure of the internal waves and tides in the tropical Pacific: here we plot the hourly mean Eulerian vertical velocity at the start of 1996 on a section south of Hawaii at 167°W from the Equator to 30°N. For reference, the Hawaiian Archipelago lies between 18.5°N and 28°N. This signal includes both the internal waves and, in the tidal simulations, the internal tide; these contributions may be distinguished by the absence of the internal tide signal in the non-tidal simulations. It can be seen in Figures 4(a) and (d) that the NIGWs and internal waves in this configuration manifest predominantly in the first baroclinic mode, with maximum amplitudes generally occurring at between 1000m and 3000m depth in both cases; the internal tides are characterized by significantly higher vertical velocities than the NIGWs, with maximum values on this section of about 30 m day^{-1} from NIGWs (panel (a)) and more than 50 m day^{-1} from tides (panel (d)). We also note that the large Eulerian vertical velocities associated with the internal tides span almost the whole depth of the ocean, and in particular have significant magnitudes at depths of 200-500m, characteristic of the seasonal thermocline. Equatorial waves are again visible within 10° of the Equator in both experiments using the default z~ timescale parameters (panels (b) and (e)), and again they are more strongly transformed by z~ with the longer timescales (panels (c) and (f)).

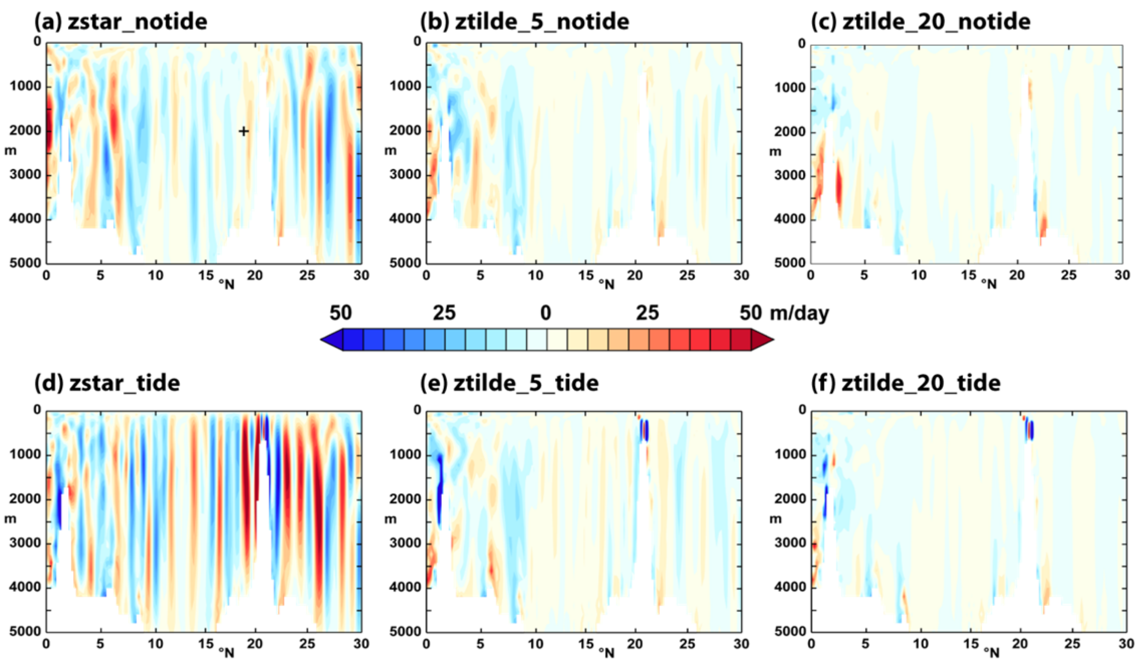

Figure 4. Hourly Eulerian vertical velocity in the Pacific on a section at 167°W from the Equator to 30°N in (a) *zstar_notide*; (b) *ztilde_5_notide*; (c) *ztilde_20_notide*; (d) *zstar_tide*; (e) *ztilde_5_tide*; and (f) *ztilde_20_tide*. The "+" in Figure 4(a) shows the position at 18°N, at which the time series displayed in Figure 5 are evaluated.

To demonstrate more quantitatively the effect of z~ on the internal waves, we show in Figure 5 ten-day time series for each experiment at a point at 18°N, 167°W, south of the Hawaiian Archipelago (the location marked by a '+' in Figure 4(a)), where large internal tide amplitudes are observed. The black curves show the Eulerian vertical velocity on the level k=55 with nominal depth 2022 m, and the red curves show the rate of change of height of the same depth coordinate level. As demonstrated by MCS2023 (albeit at a different location), the z~ coordinate successfully transforms most of the Eulerian, advective velocity associated with internal waves in the z* case (panel (a)) to coordinate displacements (panels (b) and (c)), and in the case of the longest z~ timescales the Eulerian vertical motions are reduced by more than 90%. Changing the vertical coordinate to z~ with tides again substantially reduces the Eulerian vertical velocity, and the amplitude of the residual vertical velocity signal in *ztilde_20_tide* (panel (f)) is reduced to a similar level as that in the non-tidal experiment *ztilde_20_notide*. The rate of coordinate displacement in the z~ simulations is consistently in phase with the Eulerian vertical velocity with z*, and with the timescale parameter set to 20 days has a very similar amplitude. The phase of the residual velocity (the black lines in Figures 5(b), (c), (e) and (f)) in both tidal and non-tidal simulations, however, is delayed by approximately π/2, consistent with the action of a first-order filter, as noted by Leclair and Madec (2011). This means that there is an error in the phase of the advective vertical velocity, which has potential implications for the accuracy of the vertical advection in certain regimes; this may be resolved by using a higher order filter for z~ in future configurations.

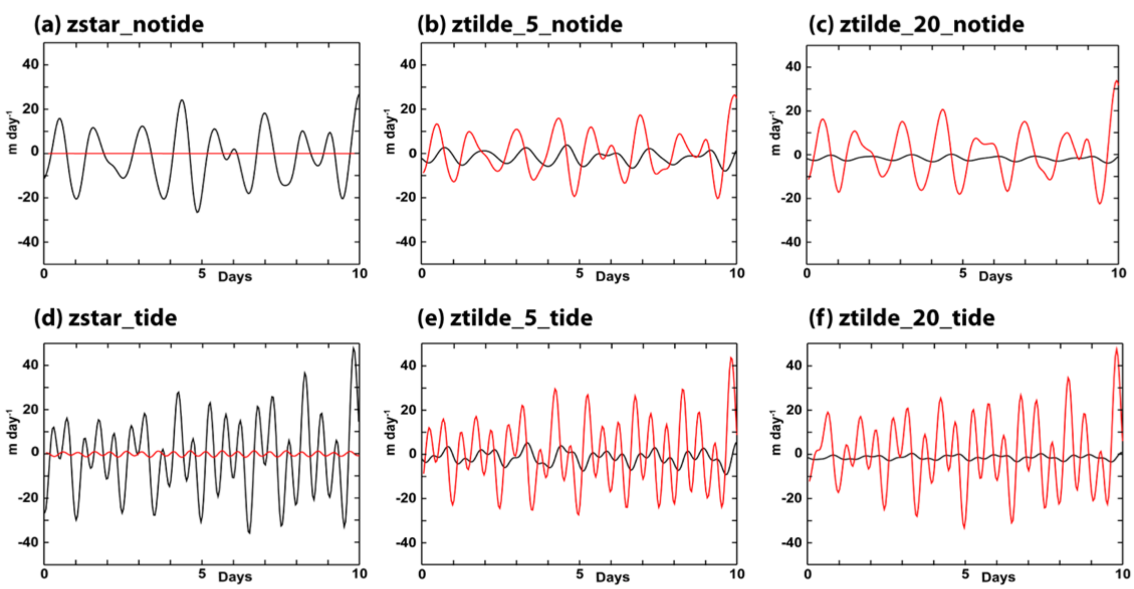

Figure 5. Hourly time series of the Eulerian vertical velocity (black) and the rate of change of height (red) of the same depth coordinate level at a point south of the Hawaiian Archipelago at 18°N, 167°W on level k=55 with nominal depth 2022m in: (a) *zstar_notide*; (b) *ztilde_5_notide*; (c) *ztilde_20_notide*; (d) *zstar_tide*; (e) *ztilde_5_tide*; and (f) *ztilde_20_tide*.

In this section, we have confirmed that the model simulates a realistic external tide; that there is an acceptably realistic internal tide field, albeit almost exclusively in the first vertical mode and with an amplitude reduced to 30-50% of that seen in observations and in higher resolution tidally forced models. We have demonstrated that the z~ coordinate functions as intended in reducing the advective Eulerian vertical velocity associated with numerical mixing by up to 90% when there is a strong internal tide; and finally that z~ preserves the internal tide, both as represented by its signature in the surface elevation and also in terms of the transformation from its representation as vertical velocities in z* simulations to coordinate displacements in simulations using z~.

4. Mixing analysis

4.1 Summary of analysis

The analysis, based on that of Lee et al (2002), is identical to that described in Megann (2018) and again used by Megann and Storkey (2019) and in MCS2022. For clarity, we shall define again in this section the main quantities that we shall evaluate in Section 4.

A density transformation streamfunction $G(\Theta,\rho)$ is defined as

$$G(\Theta,\rho) = \Psi(\Theta,\rho) + \frac{\partial}{\partial t}V(\Theta,\rho) \quad (1)$$

where $\Psi(\Theta,\rho)$ is the overturning streamfunction at latitude Θ and potential density ρ, and $V(\Theta,\rho)$ is the volume below the isopycnal surface ρ and south of Θ. Considering only the ocean interior (defined as those regions in density space with potential density higher than the maximum monthly surface density over the 10-year analysis period), and assuming that the density transformation is entirely due to diffusive processes, we define a zonal mean effective diffusivity κ_{eff} as

$$\kappa_{eff}(\Theta,\rho) = \int_{\rho_{max}}^{\rho} \frac{\partial G(\Theta,\rho)}{\partial y} d\rho \Big/ \int_{x_W}^{x_E} \frac{\partial \rho}{\partial z} dx \quad (2)$$

where x_W and x_E are the westward and eastward limits, respectively, of the basin at latitude Θ, and y is the northwards special dimension, with both x and y in meters. We note that Equations (1) and (2) neglect the contributions to the transformation rate from the nonlinearity of the equation of state, namely cabbeling and thermobaricity, which were associated by Megann (2018) with negative values of the effective diffusivity, mainly in the Southern Ocean, but also at subpolar latitudes in the North Atlantic.

We evaluate κ_{eff} in the same set of potential density classes as used by Megann (2018) from 5-day means from the final ten years of the integrations (1996 to 2005). In the experiments with z~, the total effective meridional transport, including the "thickness diffusion" correction fluxes applied when the z~ coordinate is updated, is used for the calculation of the streamfunction in place of the simple advective flux. We note that more accurate volume weighting, along with more consistent masking of ventilated density classes, has been used in the calculations of zonal and global mean quantities in this paper, and as a result the appearance of some of the figures in this section differs slightly from the corresponding figures in MCS2022.

4.2 Results of mixing analysis

In this section we use the analysis described in the foregoing section to investigate the sensitivity of the mixing, as represented by the effective diffusivity κ_{eff}, to tidal forcing and to the vertical coordinate. As a baseline for the analysis of the numerical mixing, we also compare κ_{eff} with the explicit diffusivity κ_{exp} used in the TKE mixing scheme, again evaluated as zonal means on potential density classes. We shall address two principal questions: firstly, what is the sensitivity of the numerical mixing to tidal forcing; and secondly, how does changing to the z~ vertical coordinate affect the numerical mixing?

We first look at the sensitivity of the explicit diffusivity κ_{exp} to the choice of the vertical coordinate and to tidal forcing. In Figure 6 we show the zonal mean explicit diffusivity κ_{exp}, evaluated over the last 10 years of selected simulations, along with their ratios. In the top panels we compare κ_{exp} in three experiments using z*: panels (a) and (b) show that there is relatively weak sensitivity of κ_{exp} to tidal forcing when the Simmons et al. (2004) mixing parameterisation is applied, but that when the latter is disabled (panel (c)) there is a substantial reduction in the diffusivity, especially at higher densities. Figure 6(d), showing the ratio of κ_{exp} between the non-tidal experiments z*star_notide* and *ztilde_5_notide*, confirms that z~ has little effect on the explicit diffusivity. Figure 6(e) shows the ratio of κ_{exp} between *zstar_notide* and *zstar_tide*, demonstrating that tidal forcing, perhaps counterintuitively, leads to a reduction in κ_{exp} of the order of a few percent (this will be confirmed more quantitatively in Figure 8). Panel (f) shows the reduction in κ_{exp} that results from disabling the Simmons et al. parameterization, confirming that applying the latter enhances the diffusivity in almost all locations by up to an order of magnitude, with its main contributions in deep and bottom waters with σ_2 greater than 36.8 kg m^{-3}, and also in lighter waters within a band around the Equator between 15°S and 15°N.

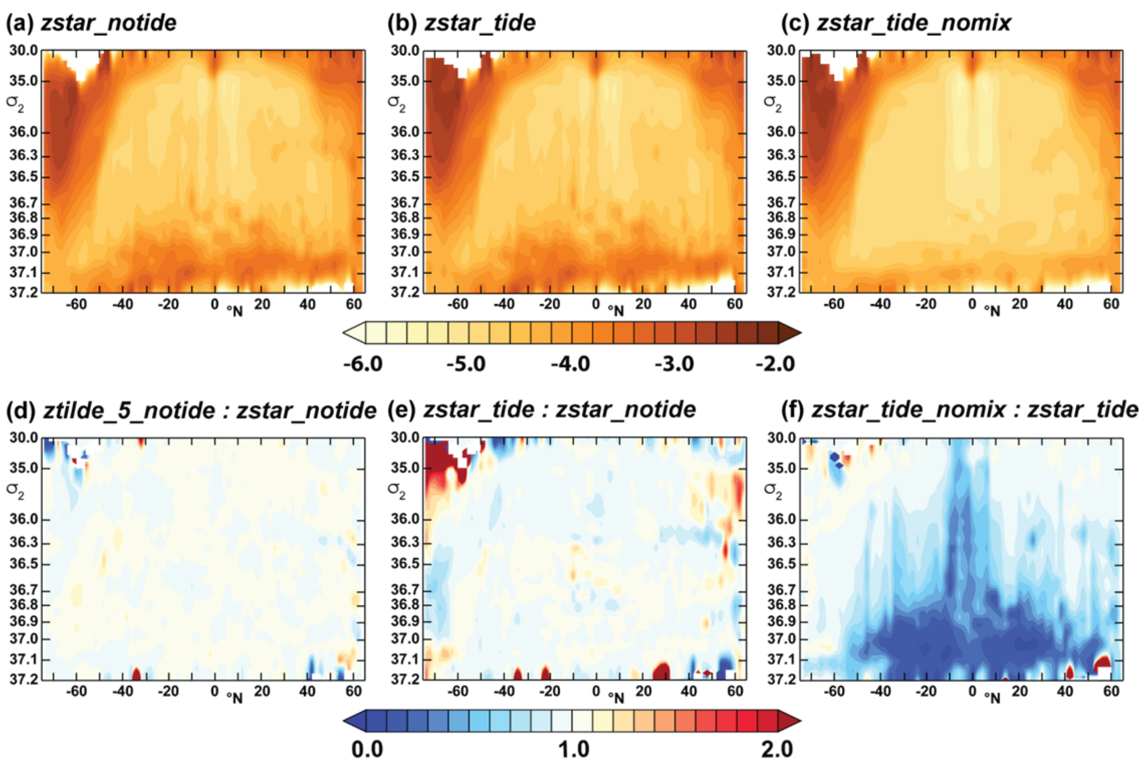

Figure 6. The logarithm of the zonal mean explicit diffusivity κ_{exp} in the global domain, plotted against latitude and potential density σ_2, in (a) *zstar_notide*, (b) *zstar_tide*; and (c) *zstar_tide_nomix*; and ratios of κ_{exp} between that in (d) *ztilde_5_notide* to *zstar_notide*; (e) *zstar_tide* to *zstar_notide*; and (f) *zstar_tide_nomix* to *zstar_tide.*

It is useful at this point to compare the explicit diffusivities shown in Figure 6 with those estimated from ocean observations. Waterhouse et al. (2014) use a range of turbulent mixing data to estimate the diffusivity κ, summarizing that κ rises to above

$5x10^{-5}$ m^2 s^{-1} in the bottom 1000 m over rough topography and ridges. Simmons et al. (2004) suggest that κ increases from ~$1x10^{-5}$ m^2 s^{-1} at intermediate depths to ~$1x10^{-4}$ m^2 s^{-1} in bottom waters. We infer that the explicit diffusivity κ_{exp} used in the present model with the Simmonds et al. parameterization (Figure 6(a)) has a distribution much closer to observed estimates than when this scheme is not applied (Figure 6(c)).

Figure 7 shows ratios of the zonal mean effective diffusivity κ_{eff}, as defined in Equation (2), between selected pairs of the experiments. The long black dashed lines indicate the maximum monthly surface density at any latitude over the analysis period; this defines the upper limits of the region of the ocean that is never part of the mixed layer, so is not subject to surface buoyancy fluxes, and in which the assumption made in Equation (2), namely that diffusion dominates density changes, is therefore expected to hold to first order. For this reason, the diffusivity is masked out in regions where the density is lower than the maximum surface density. White areas in the interior, unventilated region (principally south of 40°S and in deep waters north of 30°N) indicate negative values of κ_{eff}, which are likely to correspond to regimes where density transformation rates from cabbeling or thermobaricity are significant compared with those from diffusion. The vertical bands in Figure 7 are attributed to truncation errors from the 5-day time sampling, which produce kinks in the streamfunctions, and which are significantly reduced with this averaging period compared with the case where monthly means are used. The results for the global means of κ_{eff} in density classes that we shall present in Figure 8 will better represent large-scale changes in the effective diffusivity.

The top row (Figures 7(a)-(c)) shows the ratios of κ_{eff} in the non-tidal experiments to that in *zstar_notide*, and the second row (panels (d)-(f)) shows the corresponding ratios for the three main tidal experiments; in both cases we include for comparison the trivial unity ratio between the respective z* experiment and itself (left hand panels). In the non-tidal simulations (top panels) a general tendency is seen for z~ to reduce κ_{eff} over much of the domain, with the effect strengthening as the z~ filter timescale $\tau_{\sim}$ is lengthened from 5 days (panel (b)) to 20 days (panel (c)). A similar sensitivity to z~ is seen for the tidal simulations (panels (d)-(f)), with reductions in κ_{eff}

being found almost everywhere. The bottom row (panels (g)-(i)) shows the ratio of κ_{eff} between tidal and non-tidal experiments with each of the three vertical coordinate choices: the overall tendency is for tides to increase κ_{eff} by up to 50% within the latitude band 30°S-30°N, with the strongest increase of over 50% seen in intermediate water densities of σ_2=35.0 to 36.5 kg m^{-3}. We note that the region between 30°S and 30°N, where the largest increases in mixing are found, was identified in Section 3.2 as the location of the strongest semidiurnal internal tides, as well as being the latitude range in which the diurnal internal tides are able to propagate.

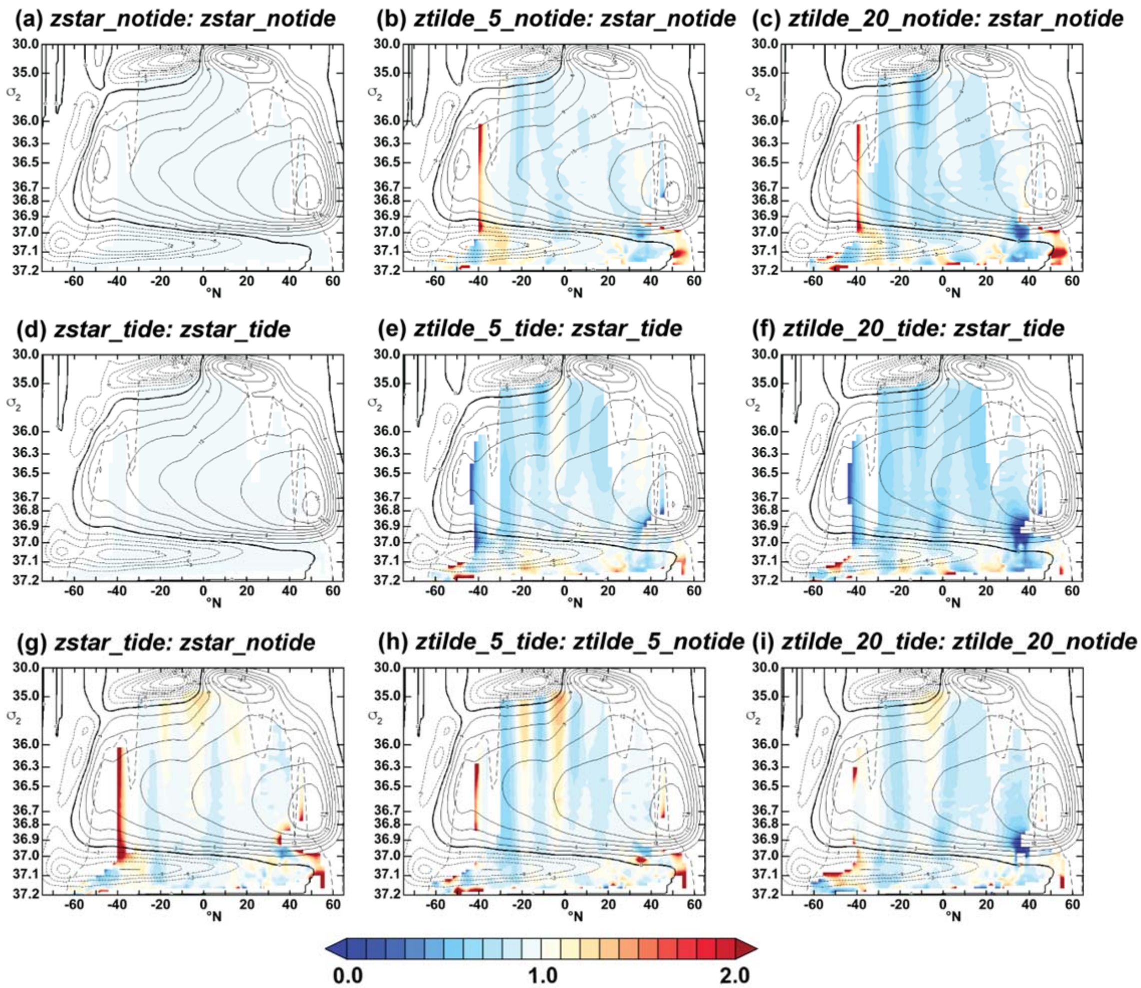

Figure 7. Ratios of the effective diffusivity κ_{eff} in the global domain to that in *zstar_notide*, plotted against latitude and potential density σ_2. Ratios to *zstar_notide of:* (a) *zstar_notide*; (b) *ztilde_5_notide*; (c) *ztilde_20_notide*; ratios to *zstar_tide of:* (d) *zstar_tide*; (e) *ztilde_5_tide*; and (f) *ztilde_20_tide*; and ratios between tidal and

non-tidal experiments with (g) z*; (h) z~ with a 5-day timescale; and (h) z~ with a 20-day timescale. The long dashed black lines show the maximum monthly surface density over the analysis period, and the black contours are of the global overturning streamfunction. Values of κ_{eff} are masked out where the density is less than the maximum monthly surface density at that latitude.

To compare more quantitatively the sensitivity of the explicit and effective diffusivities to tidal forcing and to the choice of vertical coordinate, Figure 8 shows the global means of the explicit and effective diffusivities in density classes; we include the two additional experiments *zstar_tide_nomix* (with the Simmons et al. mixing parameterization disabled: red line), and *zstar_notide_16m* (no tidal forcing, but with the same bathymetry as in the tidally forced experiments: cyan line) for comparison. The global means exclude the ventilated regions masked out in Figure 7. In the top panels we display the explicit diffusivity κ_{exp}: panel (a) shows κ_{exp} in m^2s^{-1} for each experiment on a logarithmic scale, and panel (b) shows the ratio of κ_{exp} to that in the *zstar_notide* control experiment. This confirms that in all cases except *zstar_tide_nomix* there is little sensitivity of the explicit diffusivity to either tidal forcing or to the vertical coordinate, although the tidally forced experiments (green traces and dashed blue trace) generally have a κ_{exp} smaller by between 2% and 5% compared with the non-tidal experiments. In *zstar_tide_nomix* (red trace), by contrast, there is a substantial reduction in the explicit diffusivity in all density classes, being about 20% of that in *zstar_tide* in intermediate waters, dropping to less than 50% in densities higher than σ_2=36.7.

Panel (c) shows the global mean κ_{eff} in each experiment, while panel (d) shows the ratio of κ_{eff} in each experiment to that in *zstar_notide*. It can be seen that applying tidal forcing to z* (solid green line) increases κ_{eff} in density classes between σ_2=34.0 and 36.3 kg m^{-3}, corresponding broadly to intermediate waters, consistent with the patterns seen in Figures 7(g)-(i). Enabling z~ in non-tidal simulations gives a modest reduction in κ_{eff} that increases from 5-10% with a 5-day filter timescale (black dashed lines) to 10-15% (magenta dashed line) with a 20-day timescale. In the presence of tidal forcing, however, the sensitivity to z~ is amplified: a 5-day timescale (green dashed lines) reduces κ_{eff} by more than 10% relative to *zstar_tide*, while z~ with a

20-day timescale (blue dashed lines) produces a reduction in κ_{eff} of more than 20%. As a result, the combination of tides and z~ with a 20-day timescale has, perhaps surprisingly, between 15 and 30% less mixing than with the non-tidal z* simulation *zstar_notide*, with the largest reductions at densities between σ_2=36.5 and 36.7 kg m^{-3}, typical of Upper North Atlantic Deep Water, and between σ_2=36.9 and 37.1 kg m^{-3}, corresponding to bottom waters. Disabling the Simmons et al. mixing parameterization in *zstar_tide_nomix* (solid red line in panels (c) and (d)) gives a robustly smaller κ_{eff} than in *zstar_tide* (solid green line), which is chiefly attributed to the reduction in the baseline physical mixing.

We note that in some density and latitude ranges the effective diffusivity is less than the explicit diffusivity; in particular, at densities greater than σ_2=36.9 the effective diffusivity is generally larger than κ_{exp}., corresponding to values less than unity in panel (e). This is likely to result at least partially from the small κ_{eff} values close to the zero crossing between 40°S and 50°S (negative values are masked in these figures), which correspond to the large positive and negative ratios in this region seen in Figure 7, particularly at densities greater than σ_2=36.9. This could be addressed in future studies by explicitly including the contributions to density transformations from cabbeling and thermobaricity in Equations (1) and (2).

Finally, we note that the deepening of the bathymetry found to be necessary for the tidally forced simulations is seen to have a negligible effect on either the explicit or effective diffusivities when applied to the non-tidal experiment *zstar_notide_16m* (solid cyan curves in Figure (8)).

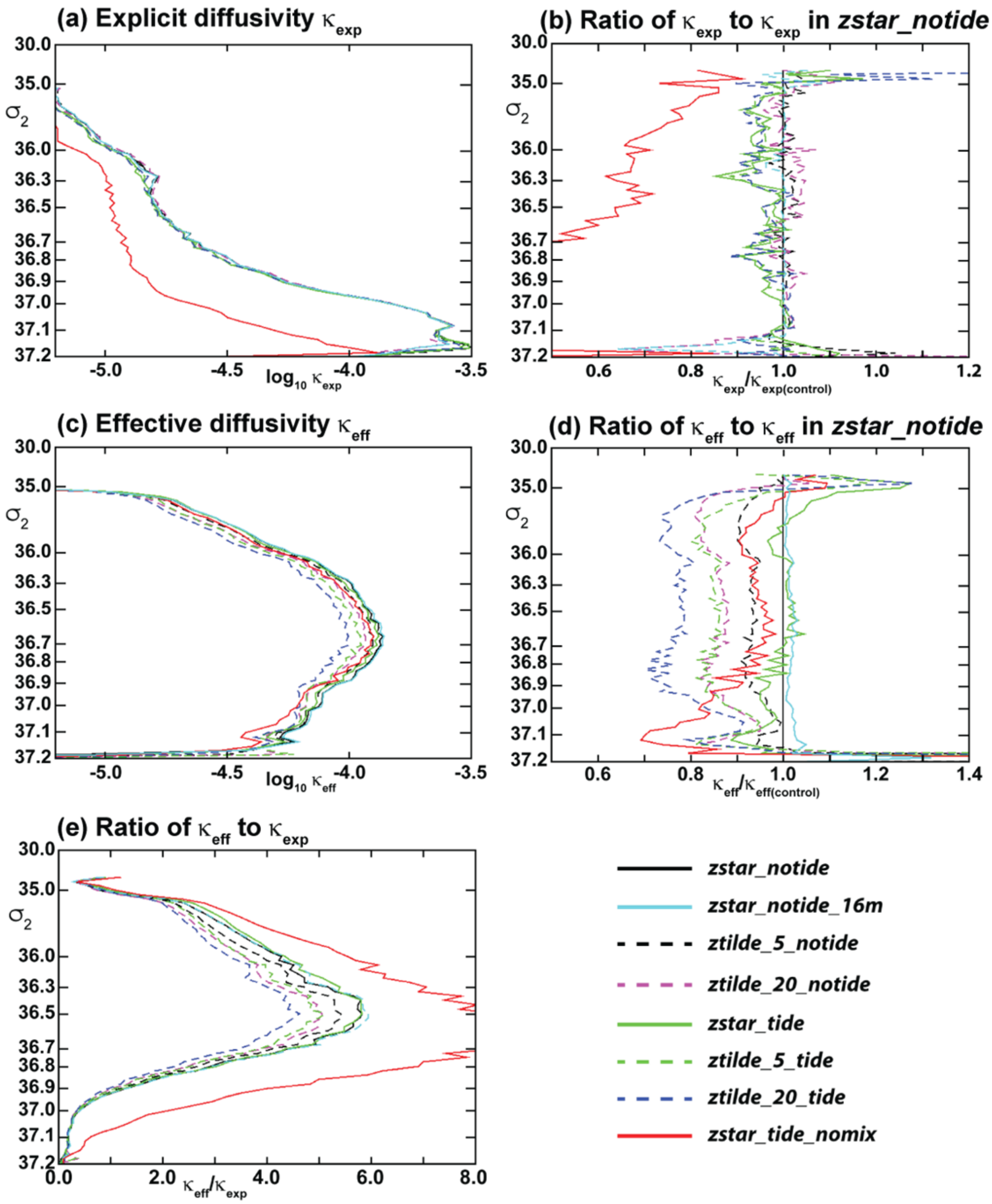

Figure 8. Global volume-weighted mean diffusivities and their ratios, evaluated in potential density classes: (a) log of global mean explicit diffusivity κ_{exp} ($m^2 s^{-1}$); (b) ratios of global mean explicit diffusivity κ_{exp} to that in *zstar_notide*; (c) log of global mean effective diffusivity κ_{eff} ($m^2 s^{-1}$); (d) ratios of κ_{eff} to that in *zstar_notide*; (e) ratios of effective diffusivity κ_{eff} to the respective explicit diffusivity κ_{exp}.

5. Sensitivity of model fields to z~ and tidal forcing

5.1 Changes in thermocline stratification

Changes in net mixing would be expected to manifest as changes in the density stratification. As a measure of the stratification, we use the square of the buoyancy frequency $N^2 = -\frac{g}{\rho_0}\frac{\partial\rho}{\partial z}$, where g=9.81 m s^{-2} and ρ_0=1035 kg m^{-3}. In Figure 9 we show the ratios of this quantity between each experiment and that in *zstar_notide*, evaluated in each case from monthly means over the ten-year analysis period at the thermocline depth, here defined as the maximum value of N^2 in the upper 1,000 meters. In the non-tidal experiments (panels (a)-(c)), the sensitivity of N^2 at the thermocline to z~ is relatively weak over most of the ocean, with the exception being a marked increase in the northwest Atlantic and changes of both signs in the Southern Ocean. This is qualitatively consistent with Figures 7(b) and (c), which show that the effective diffusivity just below the ventilated region, shown by the black dashed lines, is relatively weakly sensitive over much of the ocean to the choice of vertical coordinate. Tidal forcing (panels (d)-(f)) consistently reduces the stratification in the thermocline by 10-20% with the exception again being in the Southern Ocean, with the largest large-scale reductions seen between 30°S and 30°N; this is the latitude range where the maximum internal tide is found (Figure 2), as well as where an increase in κ_{exp} was noted in Figures 7(g)-(i). To summarize, the effect of tides is principally to reduce the stratification at the thermocline, and changing from z* to z~ increases the stratification.

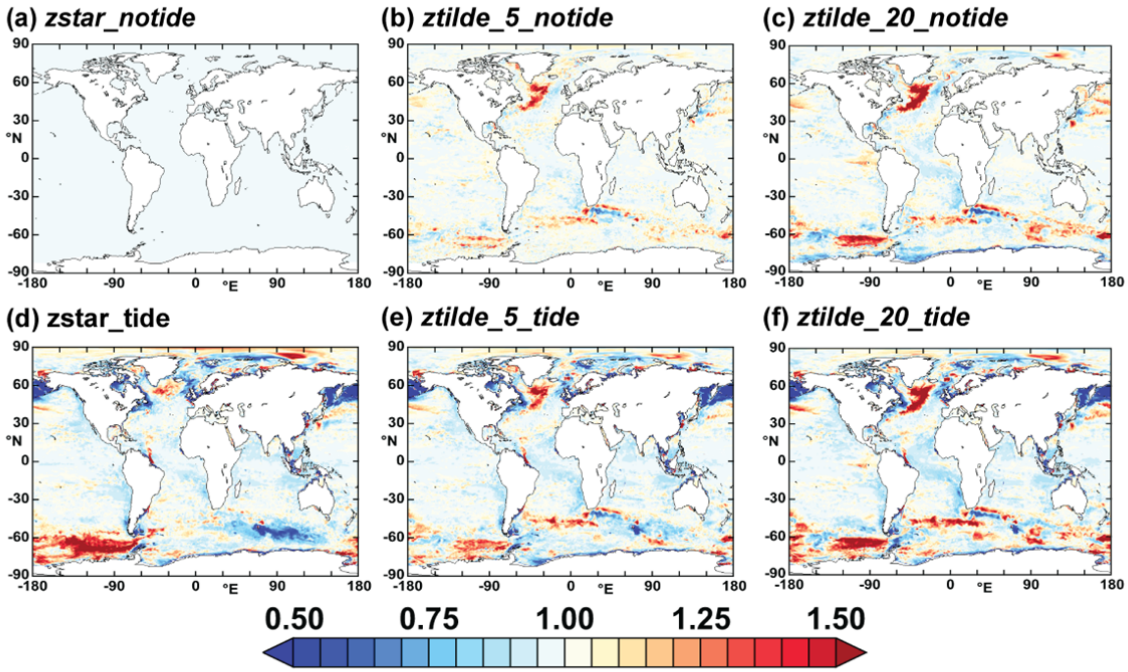

Figure 9. Ratios of the square of the buoyancy frequency N^2 at the depth of the thermocline to that in *zstar_notide* of (a) *zstar_notide*; (b) *ztilde_5_notide*; (c) *ztilde_20_notide*; ratios to *zstar_tide of* (d) *zstar_tide*; (e) *ztilde_5_tide*; and (f) *ztilde_20_tide.*

5.2 Temperature biases and drifts

MCS2022 demonstrated a robust correlation between the level of numerical mixing and zonal mean temperature biases, with reductions in the former consistently reducing the latter. This reduction was most pronounced at a depth of 300-500m, typical of the seasonal thermocline; in that ensemble, lengthening the z~ time scales led to progressively increased warming at mid-latitudes and cooling in the North Pacific and Southern Ocean, with both these tendencies opposing the large-scale biases in the z* control. Figure 10 shows the zonal mean temperature bias in the present ensemble, averaged over 1996-2005 with respect to the EN4 climatology (Good et al, 2013) at selected depth levels, which may be compared directly with Figure 8 of MCS2022. The effect of z~ in the non-tidal experiments (black and magenta lines) is to reduce both the cold bias between 30°S and 30°N and the warm bias between 30°N and 60°N; the effect is similar in magnitude at 300m and 500m and less at 1000m, and weak at the surface and deeper than 1000m. The effect of tidal forcing with both z* and z~ (green and blue curves) is, perhaps surprisingly, to further oppose the biases in these same depth ranges, with a strong additional warming of 0.3-0.4K between 30°S and 30°N at 300m and a cooling by a similar amount between 40°N and 60°N. The combination of tides and z~ (green and blue dashed lines) gives the largest change from *zstar_notide*, with *ztilde_20_tide* in fact reversing the sign of the bias at low latitudes to give a slightly positive zonal mean bias. At latitudes north of 70°N, tidal forcing in the z* case causes a significant warm bias at depths between 300m and 2000m (solid green lines in Figures 10(b)-(d)) that is strongly reduced by z~, which reduces the mean biases to close to zero.

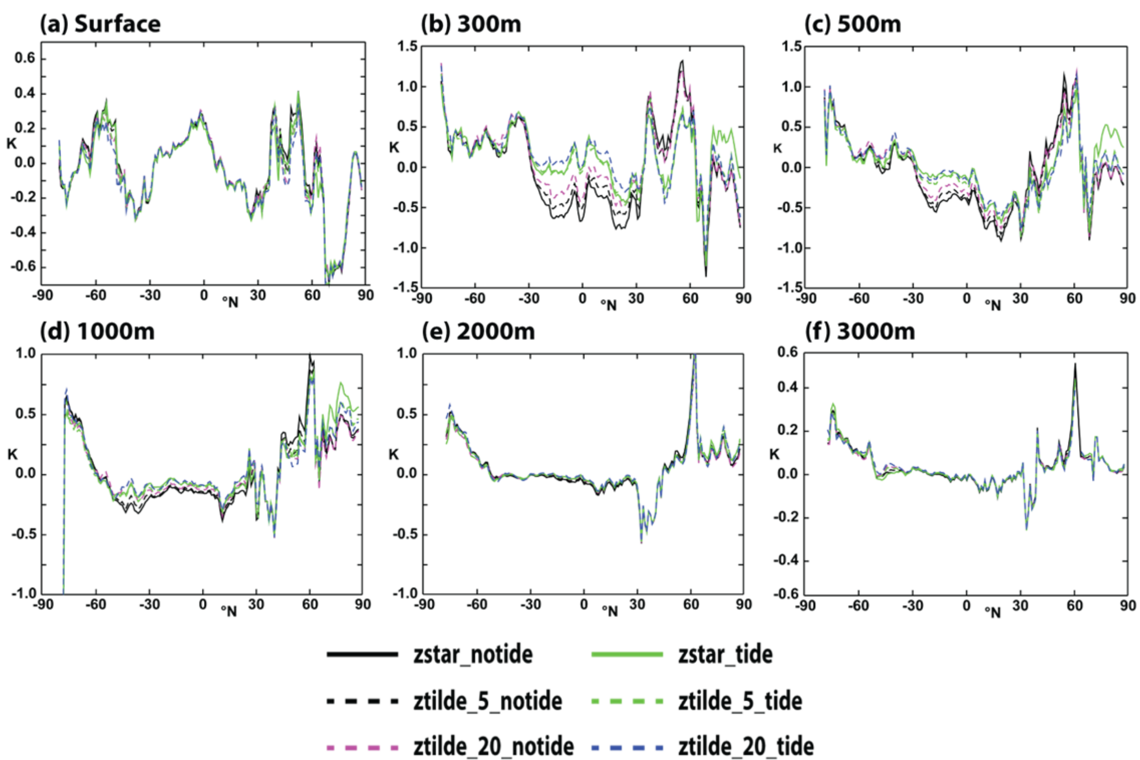

Figure 10. Zonal mean temperature biases at selected depth levels, with respect to the mean over the same time period in the EN4 climatology: (a) surface; (b) 300m; (c) 500m; (d) 1000m; (e) 2000m; and (f) 3000m.

Table 3 lists the global RMS biases on each of these depth levels, as well as the ratio of the respective standard deviation to the ensemble mean at each depth. At the surface the biases differ by less than 1% across the ensemble: this lack of sensitivity is mainly due to the feedback imposed from the surface heat flux onto the SST through the bulk formulae. At 3000m the biases and the variation across the ensemble are again small. At other depth levels, these figures confirm the pattern observed qualitatively earlier in the section: firstly, that the biases consistently reduce from *zstar_notide* to *ztilde_5_notide and further* to *ztilde_20_notide*, and secondly that tidal forcing further reduces the biases, although among the tidally forced experiments the sensitivity to the vertical coordinate is not significant.

Run	0m	300m	500m	1000m	2000m	3000m
zstar_notide	0.569	0.807	0.619	0.316	0.130	0.095
ztilde_5_notide	0.568	0.766	0.602	0.302	0.124	0.091
ztilde_20_notide	0.567	0.742	0.587	0.295	0.120	0.089
zstar_tide	0.559	0.747	0.552	0.285	0.124	0.090
ztilde_5_tide	0.566	0.720	0.555	0.296	0.122	0.088
ztilde_20_tide	0.569	0.724	0.554	0.293	0.127	0.092
Standard dev (% of zstar_notide mean)	0.6%	3.7%	4.5%	3.2%	2.7%	2.3%

Table 3. Global RMS temperature biases in K with respect to the EN4 climatology in years 1996-2005

To display the spatial structure of the changes from z~ and tides, and to confirm the consistency of the reduction in temperature bias, Figure 11 shows the biases in the z* control *zstar_notide* at 300m and 2000m, and the changes at the same depths in each of the other five simulations relative to *zstar_notide*. At 300m (Figure 11(a)) large-scale warm biases of up to +-2K are clearly visible in the subpolar gyres of the Pacific and Atlantic and in the Southern Ocean, along with cold biases of similar magnitude in the subtropical and tropical regions. The exception to the latter is the Indian Ocean, where there is a warm bias of around 0.5K. Enabling z~ (Figures 11(b) and (c)) partially reverses these biases, with a relatively stronger effect in the subtropical and tropical Atlantic, and lengthening the z~ timescales (Figure 11(c)) gives a stronger reduction than with the default settings. As remarked by MCS2022, z~ causes an enhancement of the cold bias off Newfoundland, which may be related to partial cancellation of a structural error related to the 1/4° resolution (e.g. Marzocchi et al., 2015). Adding tidal forcing to z* (Figure 11(d)) leads to a warming of almost 1K in those tropical and subtropical regions where *zstar_notide* shows a cold bias, with larger changes seen in the tropical Pacific, where z~ alone has a relatively weak effect. At this depth tidal forcing also has a cooling effect of 0.5-1.0K across the whole latitude band between 30°N and 60°N where *zstar_notide* is biased warm. Enabling z~ with tidal forcing (Figures 11(e) and (f)) combines the effects of the two changes almost linearly: in the South Atlantic and the tropical Pacific, *ztilde_20_tide* robustly shows the largest reduction in the biases with respect to those in *zstar_notide*. In the Arctic, tidal forcing introduces a warming that almost cancels the cool bias of between 0.5 and 1.0K in the Arctic in *zstar_notide* (Figure 11(d)), while the combination of tides and z~ in *ztilde_20_tide* (Figure 11(f)) results in little change compared to that in *zstar_notide*. The temperature at 300m in the Southern Ocean has a relatively weak sensitivity to either tides or z~, although comparison of Figure 11(f) with Figure 11(a) confirms that the overall cooling of about 0.5K from the combination of tides and z~ with $\tau_{\sim}$=20 days still opposes the warm bias in *zstar_notide*.

At 2000m similar responses to z~ and tidal forcing are seen, albeit to a much lower extent: the biases in *zstar_notide* (Figure11(g)) have a similar overall structure, being up to 1K warmer than EN4 in the Arctic and the Southern Ocean and 0.2-0.3K cooler in the Pacific and Indian Oceans and in the North Atlantic, although while at 300m the South Atlantic region is over 1K cooler than the climatology at 2000m it shows a warm bias of 0.2-0.4K. The changes in temperature at 2000m depth with tidal forcing and z~ are similar in spatial extent, if again weaker, to those at 300m, and again generally tend to oppose the biases in the *zstar_notide* control. The exceptions are in the South Atlantic and in the Arctic, where the warm bias in the control is enhanced in *ztilde_20_tide*. In contrast to the case at 300m, z~ does not strengthen the biases in the North Atlantic subpolar gyre at 2000m.

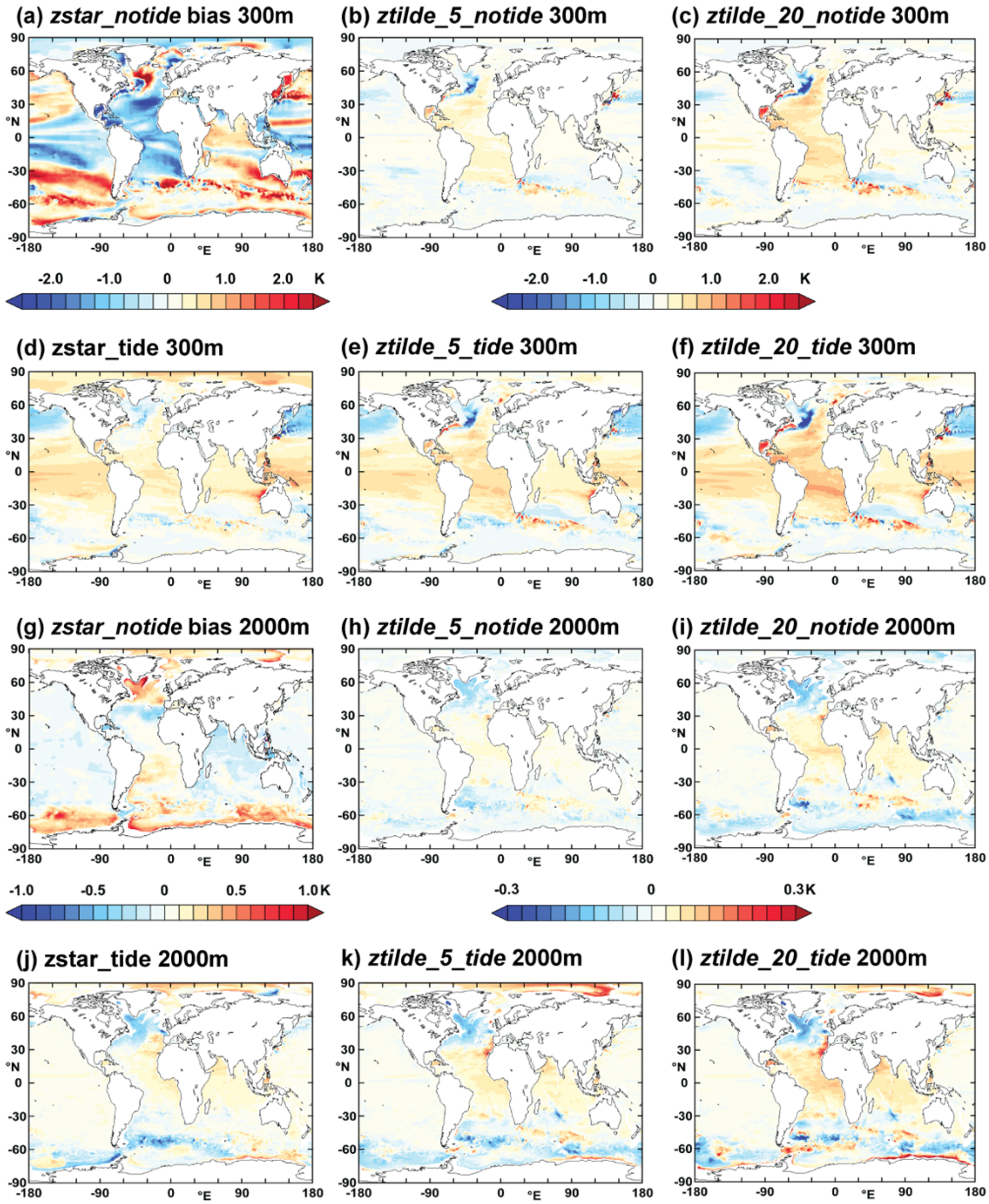

Figure 11. Temperature biases in K, averaged over 1996-2005, at two selected depth levels, and the sensitivity of the temperature to z~ and tidal forcing. (a) the temperature bias at 300m in *zstar_notide* with respect to the EN4 climatology; the temperature change at 300m from *zstar_notide* in (b) *ztilde_5_notide*; (c) *ztilde_20_notide*; (d) *zstar_tide*; (e) *ztilde_5_notide*; and (f) *ztilde_20_tide.* (g) the temperature bias at 2000m in *zstar_notide* with respect to the EN4 climatology; the temperature change at 2000m from *zstar_notide* in (h) *ztilde_5_notide*; (i)

ztilde_20_notide; (j) *zstar_tide*; (k) *ztilde_5_notide*; and (l) *ztilde_20_tide.* The left-hand color legends apply to the temperature biases with respect to climatology at the respective depth, and those at center right apply to the temperature changes with respect to the *zstar_notide* control experiment.

5.2 Large-scale circulation

MCS2022 demonstrated that implementing z~ with progressively longer timescale parameters led robustly to a weakening by up to 1.5 Sv in the maximum overturning circulation (AMOC) at 26°N, which was well correlated with the global mean of the effective diffusivity κ_{eff} for each selection of the timescale parameters. This was interpreted as a causal link between the strength of mixing in both mid-latitudes and the Southern Ocean and the strength of the overturning (in other words, a larger rate of mixing is associated with a stronger AMOC), which has been recognized through modelling and observational studies for several years (Bryan 1987; Scott and Marotzke 2001; Webb and Suginohara, 2001; Cimoli et al. 2023). Figure 12(a) and (b) show the evolution of the AMOC strength at 26°N and 45°N in the present ensemble, while columns 2 and 3 of Table 4 list the mean strength of the AMOC at these latitudes over years 21-30 of each of the integrations. The sensitivity to tides and the choice of vertical coordinate is clearer at 26°N than at 45°N; at the former latitude, there is a clear tendency for the overturning to weaken, both with and without tides, as the z~ timescales are lengthened: in both *ztilde_20_60_notide* and *ztilde_20_60_tide* there is a weaking of the AMOC by about 6% compared with the respective z* experiment. The difference between non-tidal and tidally forced experiments, with corresponding choices of the vertical coordinate, are much smaller. It is of interest to note that the experiment *zstar_tide_nomix* with the Simmonds et al. mixing parameterization disabled (cyan line) has an AMOC strength at 26°N that is close to that in *zstar_tide*, which suggests that either other interior processes besides mixing influence the overturning strength, or that the mixing that strengthens the overturning occurs in regions where the enhancements to the diffusivity contributed by the tidal parameterization scheme are not large.

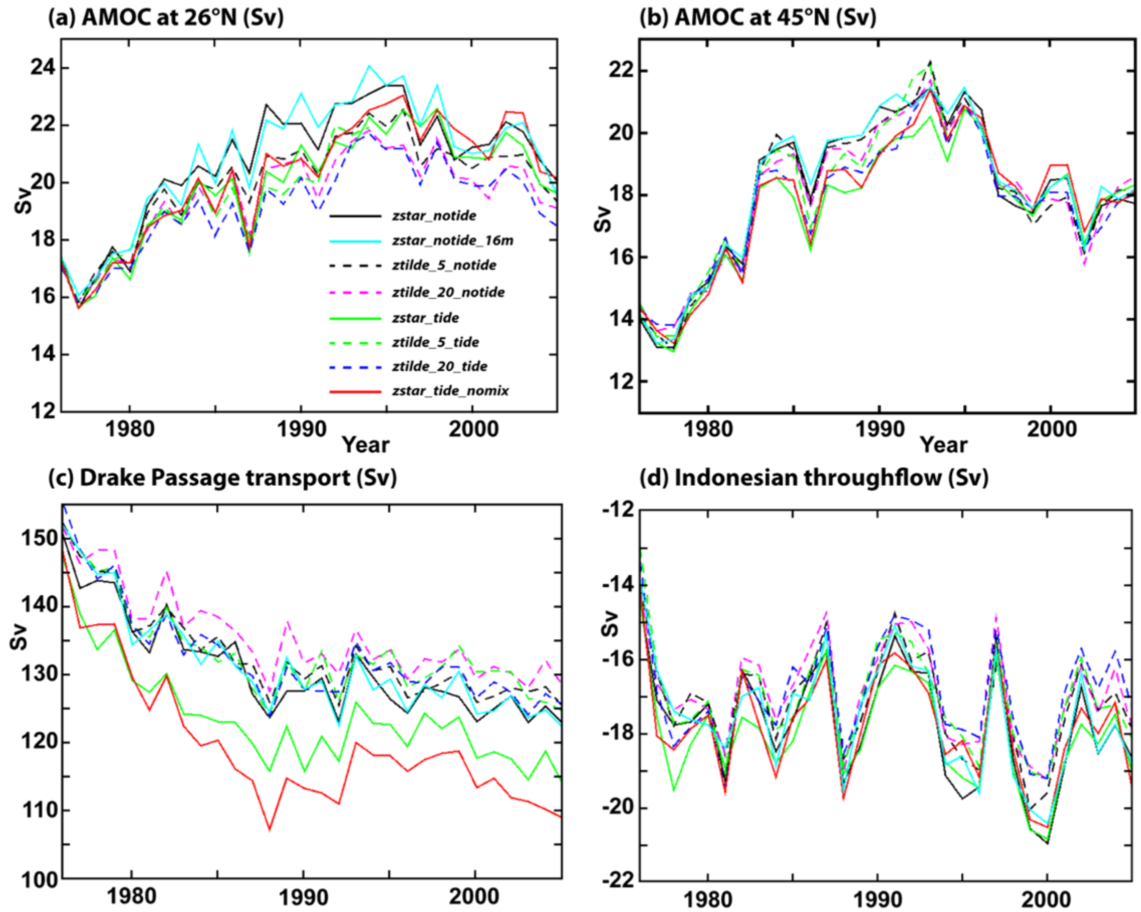

Figure 12. Large-scale annual circulation indices in Sv in the model simulations: (a) overturning strength at 26°N; (b) overturning strength at 45°N; (c) transport through Drake Passage; and (d) Indonesian throughflow.

	AMOC at 26°N	**AMOC at 45°N**	**ACC transport**	**ITF**
zstar_notide	21.50	18.03	125.3	-18.6
ztilde_5_30_notide	20.78	17.91	127.5	-17.9
ztilde_20_60_notide	20.22	18.01	130.7	-17.5
zstar_tide	21.21	18.12	119.1	-18.7
ztilde_5_30_tide	20.91	19.81	129.2	-17.7
ztilde_20_60_tide	20.02	17.86	128.0	-17.2
zstar_tide_nomix	21.65	18.33	114.1	-18.5

Table 4. Circulation indices in the model simulations, evaluated from annual means over the period 1996-2005: overturning strength at 26°N; overturning strength at 45°N; Antarctic Circumpolar Current (ACC) transport through Drake Passage; and Indonesian Throughflow (ITF), all in Sv.

The Antarctic Circumpolar Current (ACC) transport through the Drake Passage in *zstar_notide* (the solid black line in Figure 12(c)) spins down from the first year by about 25 Sv over the 30-year integration, while in the absence of tidal forcing z~ consistently reduces the spindown by between 3 and 5 Sv. Adding tidal forcing (green solid line) substantially weakens the transport, but z~ in this case reverses the weakening, and in *ztilde_20_ tide* the ACC is about 3 Sv stronger than in the *zstar_notide* control (Table 4). Disabling the tidal mixing parameterization (solid cyan line leads to the weakest ACC transport of the ensemble; the reasons for this are probably complex, as mentioned above. We conclude that applying tidal forcing to this configuration along with z~ with a 20-day timescale gives a modest improvement to the ACC transport, which is comparable to the ~3Sv of strengthening reported by Megann and Storkey (2021) when the viscosity was increased in a similar configuration.

The total throughflow through the Indonesian Archipelago (ITF) from the Pacific to the Indian Ocean between 2004 and 2006 was estimated under the INSTANT observational program to be 15.0 Sv with a seasonal cycle of about 2 Sv (Sprintall et al., 2009). Sasaki et al. (2018) report an increase in the ITF in a 0.1° near-global model when a tidal mixing parameterization is applied. Katavouta et al. (2022) used a 1/12° regional NEMO model to investigate the sensitivity of the Indonesian throughflow to tidal forcing, reporting a small increase in throughflow of about 1 Sv with tides, and conclude that the main contribution to the change in the net transport arose from interactions between the barotropic tide and the mean stratification in the straits. In the *zstar_notide* control experiment the mean ITF (see Figure 12(d) and Table 5) is 18.6 Sv; this suggests that the throughflow is a little stronger than the observational estimate, but the significant interannual variability of about ±2 Sv seen in the simulations makes direct comparison with the three-year INSTANT observational time series less useful. Adding tidal forcing with z* slightly strengthens the ITF by 0.7%, while z~ consistently weakens the transport by between 5% and 7.5%. These results are consistent with the modelling studies cited above, and we conclude firstly that tidal motions strengthen the ITF by increasing mixing, mainly due to the barotropic tide; and secondly that z~ weakens it by reducing numerical mixing.

5.3 Sensitivity of sea ice to tides and z~

As noted in the Introduction, sensitivity of the seasonal sea ice extent to tidal forcing has been reported in polar regions in model studies (e.g. Luneva et al., 2015). Figure 13 shows the mean seasonal cycle of ice extent and volume, averaged over the ten-year period 1996-2005, in the northern and southern hemispheres, along with estimated observational bounds (±20%) from the HadISST climatology (Rayner et al., 2003) for ice extent, and from the PIOMAS reanalysis (Zhang and Rothrock, 2003) for ice volume (Northern hemisphere only), respectively. The *zstar_notide* control, like the preceding GO6 configuration (see Figure 13 of Storkey et al., 2018) has a realistic winter sea ice cover in both hemispheres (the solid black line in Figures 13(a) and (b)), compared with observations, but excessively low sea ice extent in the summer, whereas the sea ice in the Arctic is too thin all year round, as evidenced by the sea ice volume (Figure 14(c)), which is below the lower observational bound for almost all months. The effect of tides (green and blue lines in Figure 13) is to reduce the ice cover in the Arctic, but the sensitivity is weak, with a reduction of less than 4% in the March ice cover in the Arctic in *zstar_tide* relative to that in *zstar_notide*, and less than 1% in the September ice cover in the Antarctic. The sensitivity to tides of the northern hemisphere sea ice volume is negligible, as is that of both the extent and volume in the southern hemisphere (Figures 13(b) and (d)). Finally, none of the metrics is significantly affected by changing to z~: for example, winter sea ice extent in both hemispheres is changed by less than 0.1% between *zstar_notide* and *ztilde_20_notide*.

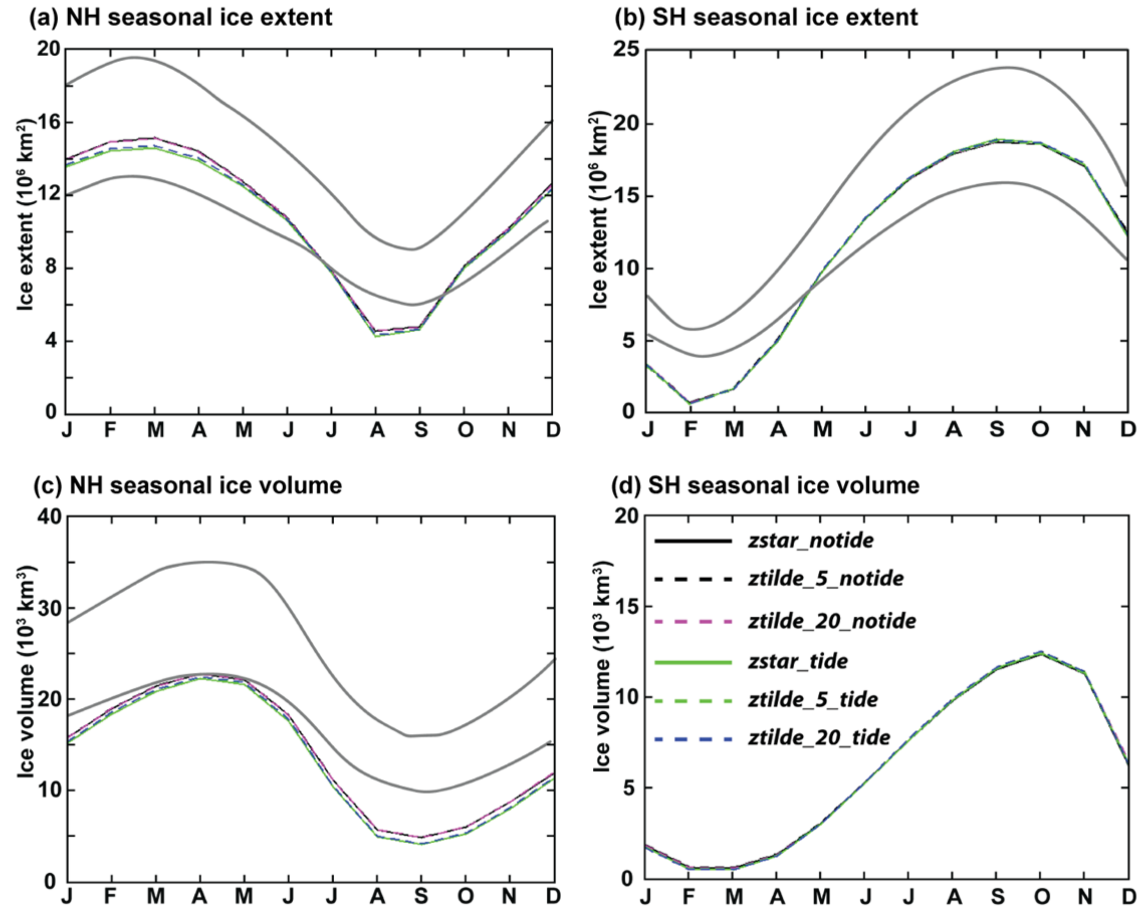

Figure 13. Mean seasonal cycle of monthly sea ice extent and thickness over 1996-2005 of the main ensemble: ice extent in km^2 in the (a) northern and (b) southern hemispheres; and ice volume in km^3 in the (c) northern and (d) southern hemispheres. The grey solid lines indicate the estimated observational bounds, derived from the respective dataset as described in the text.

5. Summary and discussion

We have implemented tidal forcing, using the five harmonics M2, S2, N2, O1 and K1, in a global forced 1/4° NEMO configuration, and have created an ensemble of simulations with the aim of assessing the numerical mixing due to the tides. We have included for comparison both the default z* geopotential coordinate and the filtered arbitrary-Lagrangian-Eulerian z~ coordinate, which represents the vertical motions of internal waves with period of less than a few days as displacements of the coordinate surfaces, rather than as advective vertical velocities relative to the coordinate surfaces, and which has previously been shown to significantly reduce numerical mixing from internal waves in non-tidal simulations. We have confirmed that the external tide, represented by harmonics of the surface elevation at the tidal forcing frequencies, is acceptably realistic in amplitude and phase in all the simulations, despite the relatively low horizontal resolution. We have analyzed the internal tide, as represented by its signature in the surface elevation, and confirmed that this is broadly similar to that seen in satellite altimetry and in high-resolution tidal models, albeit being significantly weaker than that in either of the latter, and that its propagation away from the generation regions is realistically represented. Finally, the amplitude and spatial structure of the surface signature of the internal tides are not significantly affected by the choice of vertical coordinate in the model.

We have examined the internal structure of the internal tides in the simulations and its sensitivity to the vertical coordinate: they are present almost exclusively in the first vertical mode, as expected, given the horizontal resolution of the model grid, and are characterized in the z* case by a maximum vertical velocity at around 2000 meters depth. When the z* vertical coordinate is replaced by z~, the Eulerian vertical velocity corresponding to the internal tide is progressively transformed into displacements of the coordinate surface as the z~ timescale is lengthened, and with a 20-day timescale the Eulerian velocity from tidal motions is reduced to less than 10% of its amplitude with z*.

The effects of tidal forcing and of the choice of vertical coordinate on mixing were quantified using a mixing analysis based on density transformation rates to derive an effective diapycnal diffusivity κ_{eff} for each of the experiments. In summary, tidal forcing in the z* experiments led to an increase of up to 20% in the effective diffusivity in density classes corresponding to thermocline and intermediate waters and at latitudes between 30°S and 30°N, where a strong internal tide is present, but changing to the z~ vertical coordinate produced a strong reduction in diagnosed mixing both with and without tides and, perhaps surprisingly, the experiments with tides and z~ showed effective diffusivities between 15% and 25% lower than in the non-tidal z* control experiment over intermediate and deep water densities. The sensitivities of temperature biases at 300 m and 2,000 m depths with respect to the EN4 climatology were broadly consistent with those of the mixing diagnostics: the cool biases at 300 m between 30°S and 30°N in the control were reduced by more than 50% with tides and z~, while the warm biases between 35° and 65°N were reduced by a comparable fraction. Similar sensitivity was seen at 2,000 m depth, although the magnitudes of the biases at that depth are less than 25% of those at 300 m. With z* and tides a warm bias in the Arctic at 300m of between 0.5 and 1.0 K was present, but in all the other experiments this bias was replaced by a much smaller overall cool bias. To summarize, tidal forcing with z* increases mixing in thermocline and intermediate waters between 30°S and 30°N, reducing it slightly elsewhere, while the combination of tides and z~ reduces mixing almost everywhere, relative to that in the z* non-tidal control.

The sensitivity of the Atlantic meridional overturning circulation (AMOC) at 26°N to tidal forcing and the vertical coordinate was proportionate to those of the mixing and the temperature biases: the AMOC was strongest in the z* non-tidal control, and weakest with tidal forcing and with z~ with the longest timescale. This confirms the hypothesis of Webb and Suginohara (2001), Wunsch and Ferrari (2004) and others that mixing is a significant control on the AMOC, in the sense that stronger mixing leads to a stronger overturning circulation. The transport through Drake Passage of the Antarctic Circumpolar Current (ACC) is characterized in the non-tidal control by a gradual spindown of 25-30 Sv from the initial transport of 150 Sv. The ACC transport has the opposite sensitivity to the AMOC, with the z* non-tidal and tidal simulations having the largest spindown, and the tidally-forced experiment with a 20-day z~ timescale having the least, with the weakening reduced to about 20 Sv relative to the control. This is consistent with a hypothesis that the ACC is supported by a mean tilt of the isopycnals in the Southern Ocean, and that stronger mixing erodes this tilt and hence weakens the ACC. Finally, a small but robust dependence on tidal forcing was seen in the Indonesian throughflow, which was weakened by a few percent in the tidal experiments with z~.

Examination of the explicit and effective diffusivities with and without the Simmons et al. (2014) tidal mixing parameterization confirms that the total mixing from tidal motions, including both physical and numerical contributions, in this configuration is much lower than that provided by the parameterization, and is indeed much weaker than observational estimates for mixing. This is not surprising, since the eddy-permitting resolution used in this ensemble is far too low to simulate the higher vertical modes of the internal tide, and indeed the higher frequency internal waves that result from these internal tides, that perform mixing in the ocean. We therefore conclude that a mixing parameterization is necessary in tidally forced simulations of this resolution, which of course is typical of climate models. The Simmonds et al. scheme is not provided in standard releases of NEMO v4, and in any case has been superseded by that of de Lavergne et al. (2020), so the latter is recommended for new NEMO-based configurations.

It is not yet clear why tidal forcing with z* slightly reduces the explicit vertical diffusivity outside the 30°S-30°N latitude range, as shown in Figure 8(b), nor why the diagnosed numerical mixing and temperature biases are significantly reduced over much of the model domain when tides are present, particularly when combined with the z~ vertical coordinate. Candidates include a possible reduction by the barotropic or internal tide of the grid-scale vertical velocities associated with a computational mode at mid-depths close to western boundaries, as described by Megann (2018) and Megann et al. (2021) in related ¼° simulations, which may interact non-trivially with tidal motions; changes to viscous damping along western boundaries from the tidal currents; and changes to bottom layer thicknesses. Another possible cause could be nonlinear interactions between the internal tides and the NIGWs, which could disrupt the propagation of the latter. Further work is needed to clarify this question.

The present configuration was created to provide a working tool to explore the effects of tidal motions on numerical mixing, and is certainly not optimized to simulate a tidally-forced ocean realistically, even considering its limited resolution. Only five tidal constituents are applied, while the formulation of the bottom drag is likely to be sub-optimal in the presence of time-mean and tidal currents at the sea bottom. Work is ongoing under the Shelf-Enabled NEMO project, developed partly under the Mission Atlantic program (Artioli et al., 2023), which uses a global 1/4° NEMO v4.0 configuration closely related to that used in the present study to improve the performance of the model on the shelves without degrading the simulation in the deep ocean. The configuration used in the project, for example, applies 23 tidal forcing constituents, and has found that a modified bottom drag scheme gives considerable improvements in the representation of the barotropic tide (C. Wilson, pers. comm.). The mixing parameterization of Simmons et al. (2004) is no longer provided in the NEMO source code, and has in any case been superseded by the more sophisticated scheme of De Lavergne et al. (2020), so is not recommended for future model studies. Finally, the application of a tidal mixing parameterization scheme in the presence of resolved barotropic and low-mode internal tides is unsatisfactory, since it is likely to introduce double-counting of the contributions to mixing from these sources, so further research is needed to investigate the consequences of this.

We conclude that explicit representation of tidal motions generally improves the realism of the ¼° NEMO configuration used here, and that changing from the z* geopotential coordinate to the z~ filtered ALE coordinate further improves the performance of the model, mainly through its consistent effect in reducing numerical mixing from the internal tide. Our results suggest that investigating the effect of tidal forcing in the next generation of coupled climate models and Earth System Models will be worthwhile, providing that attention is paid to addressing numerical mixing through appropriate choice of the vertical coordinate.

Acknowledgments

This paper is dedicated to the memory of Maria Luneva, without whom the work would have been far more challenging and less satisfying. The model configurations were set up under the project “Reducing numerical mixing resulting from applying tides explicitly in a global ocean model” (RENUMERATE) under the Copernicus Marine Environment Monitoring Service (CMEMS). CMEMS is implemented by Mercator Ocean International, in the framework of a delegation agreement with the European Union. It was also funded by the Natural Environment Research Council (NERC) under the Climate Linked Atlantic Sector Science (CLASS) marine research programme, as part of the Joint Marine Modelling Programme (JMMP), part of the Joint Weather and Climate Research Programme strategic partnership between the Met Office and NERC. The model was integrated on the MONSooN system, a collaborative facility supplied under JMMP, while the analysis was carried out on the JASMIN platform, funded by NERC and maintained by the Centre for Environmental

Data Analysis (CEDA). The author is grateful to Chris Wilson for providing the FES2014 data, to Adam Blaker and Jérôme Chanut for productive discussions, and to Adrian New for useful feedback on the manuscript.

The source code for the modified GO8p0 version of the NEMO v4.0 configuration used in these integrations, along with the namelists and XML files, is archived at Zenodo: https://zenodo.org/record/6652361
The derived data used for the analysis presented here is archived at Zenodo: https://zenodo.org/record/8276604

References

Arbic, B.K., Wallcraft, A.J. and Metzger, E.J., 2010. Concurrent simulation of the eddying general circulation and tides in a global ocean model. *Ocean Modelling* **32**, 175-187. DOI: 10.1016/j.ocemod.2010.01.007

Arbic, B.K., J.G. Richman, J.F. Shriver, P.G. Timko, E.J. Metzger, and A.J. Wallcraft. 2012. Global modeling of internal tides within an eddying ocean general circulation model. *Oceanography* **25**(2) 20–29, http://dx.doi.org/10.5670/oceanog.2012.38.

Arbic, B.K., 2022. Incorporating tides and internal gravity waves within global ocean general circulation models: A review. *Progress in Oceanography* **206** (2022) 102824. https://doi.org/10.1016/j.pocean.2022.102824

Artioli, Y. et al., 2023. “Validated hindcast simulations 1980-2019 (NEMO-ERSEM & SEAPODYM)” Deliverable 6.1 from Horizons Europe Project Mission Atlantic https://missionatlantic.eu

Blaker, A.T., Hirschi, J.J.-M., Bell, M.J., and Bokota, A., 2021. Wind-Driven oscillations in the meridional overturning circulation near the equator. Part I: Numerical models. *J. Phys. Oceanog.,* **51** (3). 645-661. https://doi.org/10.1175/JPO-D-19-0296.1

Bryan, F., 1987: Parameter sensitivity of primitive equation ocean general circulation models. *J. Phys. Oceanogr.,* **17,** 970–985.

Cimoli, L., Mashayek, A., Johnson, H. L., Marshall, D. P., Naveira Garabato, A. C., Whalen, C. B., et al. (2023). Significance of diapycnal mixing within the Atlantic meridional overturning circulation. *AGU Advances*, **4,** e2022AV000800.

De Lavergne, C., Madec, G., le Sommer, J., Nurser, A. J. G., and Garabato, A. C. N. (2016). On the Consumption of Antarctic Bottom Water in the Abyssal Ocean, *J. Phys. Oceanogr.* **46**, 635–661.

De Lavergne, C., Vic, C., Madec, G., Roquet, F., Waterhouse, A. F., Whalen, C. B., et al. (2020). A parameterization of local and remote tidal mixing. *Journal of Advances in Modeling Earth Systems*, *12*, e2020MS002065. https://doi.org/10.1029/2020MS002065

Egbert, G. D. & Ray, R. D. 2001 Estimates of M2 tidal energy dissipation from TOPEX/Poseidon altimeter data. *J. Geophys. Res.* **106**, 22475–22502.

Garrett, C. J., and W. Munk, 1975: Space–time scales of internal waves: A progress report. *J. Geophys. Res.*, **80 ,** 291–297.

Gaspar, P., Grégoris, Y., and Lefevre, J.-M.: A simple eddy kinetic energy model for simulations of the oceanic vertical mixing: tests at Station Papa and long-term upper ocean study site, *J. Geophys. Res.,* **95**, 16179–16193, doi:10.1029/JC095iC09p16179, 1990.

Good, S. A., M. J. Martin and N. A. Rayner, 2013. EN4: quality controlled ocean temperature and salinity profiles and monthly objective analyses with uncertainty estimates, *JGR: Oceans*, **118**, 6704-6716.

Hogg, N.G., Biscaye P, Gardner W, Schmitz, W.J. 1982. On the transport and modification of Antarctic Bottom water in the Vema Channel. *J. Mar. Res.* **40** (Suppl.) 231–263.

Holloway, G. and Proshutinsky, A., 2007. Role of tides in Arctic ocean/ice climate. J. *Geophys. Res.* **112**. https://doi.org/10.1029/2006JC003643

Jayne, S.R., 2009. The impact of abyssal mixing parameterizations in an ocean general circulation model. *J. Phys. Oceanogr.,* **39**, 1756–1775, doi:10.1175/2009JPO4085.1.

Jourdain, N., Molines, J-M., Le Sommer, J., Mathiot, P.., Chanut, J., deLavergne, C. and Madec, G., 2019. Simulating or prescribing the influence of tides on the Amundsen Sea ice shelves. *Ocean Modelling* **133** 44-55. https://doi.org/10.1016/j.ocemod.2018.11.001

Katavouta, A., Polton, J, A., Harle, J. D., and Holt, J. T., 2022 Effect of tides on the Indonesian seas circulation and their role on the volume, heat and salt transports of the Indonesian throughflow. *J. Geophys. Res. (Oceans),* **127**

(8). https://doi.org/10.1029/2022JC018524

Koch-Larrouy, A., Madec, G., Blanke, B., and Molcard, R., 2008. Water mass transformation along the Indonesian throughflow in an OGCM. *Ocean Dynamics* **58**, https://doi.org/10.1007/s10236-008-0155-4.

Large, W. G. & Yeager, S. G., (2009). The global climatology of an interannually varying air-sea flux data set, *Clim. Dynam.,* **33**, 341–364, doi:10.1007/s00382- 008-0441-3, 2009.

Leclair, M. and G. Madec, 2011. z~-Coordinate, an Arbitrary Lagrangian–Eulerian coordinate separating high and low frequency motions. *Ocean Modelling* **37,** 139–152.

Lee, M.-M., Coward, A.C., Nurser, A.G., 2002. Spurious diapycnal mixing of deep waters in an eddy-permitting global ocean model. *J. Phys. Oceanog.* **32**, 1522–1535.

Luneva, M.V., Y.K. Aksenov, J.D. Harle and J.T. Holt, 2015. The effects of tides on the water mass mixing and sea ice in the Arctic Ocean. *JGR-Oceans* **120** . 6669-6699

Lyard, F.H, Allain, D.J., Cancet, M., Carrère, L. and Picot, L, 2021. FES2014 global ocean tide atlas: design and performance. *Ocean Sci.,* **17**, 615–649. https://doi.org/10.5194/os-17-615-2021.

Madec, G., R. Bourdallé–Badie, P.A. Bouttier, C. Bricaud, D. Bruciaferri, D. Calvert, J. Chanut, E, Clementi, C. Coward, D. Delrosso, C. Ethé, S. Flavoni, T. Graham, J Harle, D. Iovino, D. Lea, C. Lévy, T. Lovato, N. Martin, S. Masson, S. Mocavero, J. Paul, C. Rousset, D. Storkey, A. Storto and M. Vancoppenolle, 2019. NEMO Ocean Engine. doi:10.5281/zenodo.1464816

Marzocchi, A.; Hirschi, J.J.-M.; Holliday, N.P.; Cunningham, S.A.; Blaker, A.T.; Coward, A.C., 2015 The North Atlantic subpolar circulation in an eddy-resolving global ocean model. *Journal of Marine Systems*, **142**. 126-143. https://doi.org/10.1016/j.jmarsys.2014.10.007

Megann, A., 2018. Estimating the numerical diapycnal mixing in an eddy-permitting ocean model. *Ocean Modelling* **121**, 19-33. DOI: 10.1016/j.ocemod.2017.11.001

Megann, A. and D. Storkey, 2021. Exploring viscosity space in an eddy-permitting global ocean model: is viscosity a useful control for numerical mixing? *JAMES* **13**. doi: 10.1029/2020MS002263

Megann, A., Chanut, J. and Storkey, D, 2022. Assessment of the $\tilde{z}$ time-filtered Arbitrary Lagrangian-Eulerian coordinate in a global eddy-permitting ocean model. *JAMES* **14**, e2022MS003056. https://doi. org/10.1029/2022MS003056

Munk, W., and C. Wunsch, 1998: Abyssal recipes II: Energetics of tidal and wind mixing. *Deep-Sea Res*., **45**, 1977–2010, doi:10.1016/S0967-0637(98)00070-3.

Rayner, N.A., Parker, D.E., Horton, E.B., Folland, C.K., Alexander, L.V., Rowell, D.P., Kent, E.C., and Kaplan, A., 2003: Global analyses of sea surface temperature, sea ice, and night marine air temperature since the late nineteenth century, *J. Geophys. Res.-Atmos*., **108**, 4407, https://doi.org/10.1029/2002JD002670.

Ray, R.D. and Mitchum, G.T., 1997. Surface manifestation of internal tides in the deep ocean: observations from altimetry and island gauges. *Prog. Oceanog*. **40**, 35-162. https://doi.org/10.1016/S0079-6611(97)00025-6

Ray, R.D. and Zaron, E.D., 2016. M2 Internal Tides and Their Observed Wavenumber Spectra from Satellite Altimetry. *J. Phys. Oceanogr.* **46**, 3-22. https://doi.org/10.1175/JPO-D-15-0065.1

Saenko, O.A. and W. J. Merryfield, 2005: On the effect of topographically enhanced mixing on the global ocean circulation. *J. Phys. Oceanogr.,* **35**, 826–834.

Sakai, A., Senjyu, T., Matsuno, T., Tsutsumi, E. and Endoh, T., 2021. Internal waves with high vertical wavenumber structure generated by diurnal tidal flow over the eastern ridge of Luzon Strait. *J. Oceanogr* **77**, 703–718 (2021). https://doi.org/10.1007/s10872-021-00615-4

Sasaki, H., Kida, S., Furue, R., Nonaka, M. and Matsumoto, Y., 2018. An Increase of the Indonesian Throughflow by Internal Tidal Mixing in a High-Resolution Quasi-Global Ocean Simulation. *Geophys. Res. Lett.* **45**, 8416-8424. https://doi.org/10.1029/2018GL078040

Sharples, J., Tweedle, J.F., Green, J.A.M., Palmer, M.R., Kim, Y.-N., Hickman, A.E., Holligan, P.M., Moore, C.M., Rippeth, T.P., Simpson, J.H., Krivtsov, V., 2007. Spring-neap modulation of internal tide mixing and vertical nitrate fluxes at a shelf edge in summer. *Limnol. Oceanogr.* **52**, 1735–1747.

Simmons, H. L., S. R. Jayne, L. C. St. Laurent, and A. J. Weaver, 2004: Tidally driven mixing in a numerical model of the ocean general circulation. Ocean Modelling **6**, 245-263.

Song, P., Sidorenko, D., Scholz, P., Thomas, M., and Lohmann, G., 2023: The tidal effects in the Finite-volumE Sea ice–Ocean Model (FESOM2.1): a comparison between parameterised tidal mixing and explicit tidal forcing, *Geosci. Model Dev*., **16,** 383–405, https://doi.org/10.5194/gmd-16-383-2023

Sprintall, J., S. Wijffels, R. Molcard, and I. Jaya, 2009. Direct estimates of the Indonesian Throughflow entering the Indian Ocean, *J. Geophys. Res.*, **114**, C07001, doi: 10.1029/2008JC005257.

St. Laurent, L. C., and C. Garrett, 2002: The role of internal tides in mixing the deep ocean. J. Phys. Oceanogr., 32, 2882–2899, doi:10.1175/1520-0485(2002)032,2882:TROITI.2.0.CO;2.

St Laurent, L. C., Simmons, H. L., and Jayne, S. R., 2002: Estimating tidally driven mixing in the deep ocean, *Geophys. Res. Lett.,* **29**, 2106, doi:10.1029/2002GL015633.

Storkey, D., A.T. Blaker, P. Mathiot, A. Megann, Y. Aksenov, E.W. Blockley, D. Calvert, T. Graham, H.T. Hewitt, P. Hyder, T. Kuhlbrodt, J.G.L. Rae, and B. Sinha, 2018. UK Global Ocean GO6 and GO7: a traceable hierarchy of model resolutions. *Geosci. Model Dev.*, **11**, 3187–3213. DOI: 10.5194/gmd-11-3187-2018.

Tuerena, R.E., Williams, R.G., Mahaffey, C., Vic, C., Green, J.A.M., Naveira-Garabato, A., Forryan, A., Sharples, J., 2019. Internal tides drive nutrient fluxes into the deep chlorophyll maximum over mid-ocean ridges. *Global Biogeochem. Cycles* **33**, 995–1009.

Vic, C., Naveira Garabato, A.C., Green, J.A.M., Waterhouse, A.F., Zhao, Z., Melet, A., de Lavergne, C., Buijsman, M.C. and Stephenson, G.R, 2019. Deep-ocean mixing driven by small-scale internal tides. *Nat Commun* **10**, 2099. https://doi.org/10.1038/s41467-019-10149-5

Webb, D.J. and Suginohara, N., 2001. *International Geophysics* **77** 205-214. https://doi.org/10.1016/S0074-6142(01)80120-0

Wunsch, C., and R. Ferrari, 2004: Vertical mixing, energy, and the general circulation of the oceans. *Annu. Rev. Fluid Mech.,* **36**, 281–314, doi:10.1146/annurev.fluid.36.050802.122121.

Zalesak, S. T.: Fully multidimensional flux corrected transport algorithms for fluids, *J. Comput. Phys.,* **31**, 335–362, 1979.

http://dx.doi.org/10.5670/oceanog.2012.40.

Zhang, J. and Rothrock, D.A.: Modeling Global Sea Ice with a Thickness and Enthalpy Distribution Model in Generalized Curvilinear Coordinates, *Mon. Weather Rev*., **131**, 845–861, https://doi.org/10.1175/1520-0493(2003)131h0845:MGSIWAi2.0.CO;2, 2003.

Zhao, Z., 2018. The global Mode-2 M2 internal Tide. *J. Geophys. Res.,* **123**, 7725-7746. doi: 10.1029/2018JC014475

Zhao, Z., Alford, M.H., Girton, J.B., Rainville, L.and Simmons, H.L, 2016: Global Observations of Open-Ocean Mode-1 M2 Internal Tides. *J. Phys. Oceanogr.*, **46**, 1657–1684, https://doi.org/10.1175/JPO-D-15-0105.1.

Figure 1.

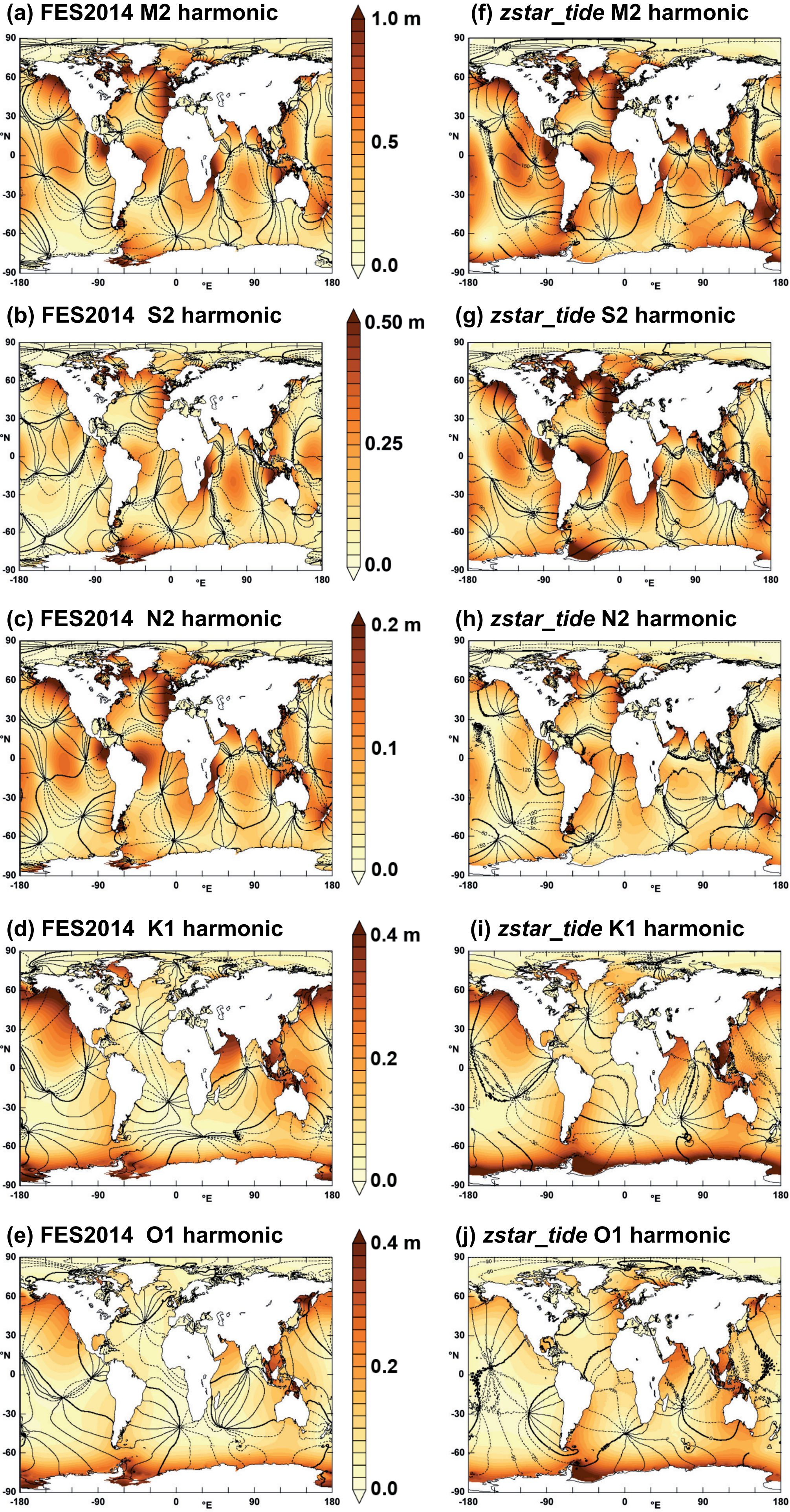
(a) FES2014 M2 harmonic
(f) zstar_tide M2 harmonic
1.0 m
0.5
0.0
(b) FES2014 S2 harmonic
(g) zstar_tide S2 harmonic
0.50 m
0.25
0.0
(c) FES2014 N2 harmonic
(h) zstar_tide N2 harmonic
0.2 m
0.1
0.0
(d) FES2014 K1 harmonic
(i) zstar_tide K1 harmonic
0.4 m
0.2
0.0
(e) FES2014 O1 harmonic
(j) zstar_tide O1 harmonic
0.4 m
0.2
0.0
°N
°E
90
60
30
0
-30
-60
-90
-180
-90
0
90
180

Figure 2.

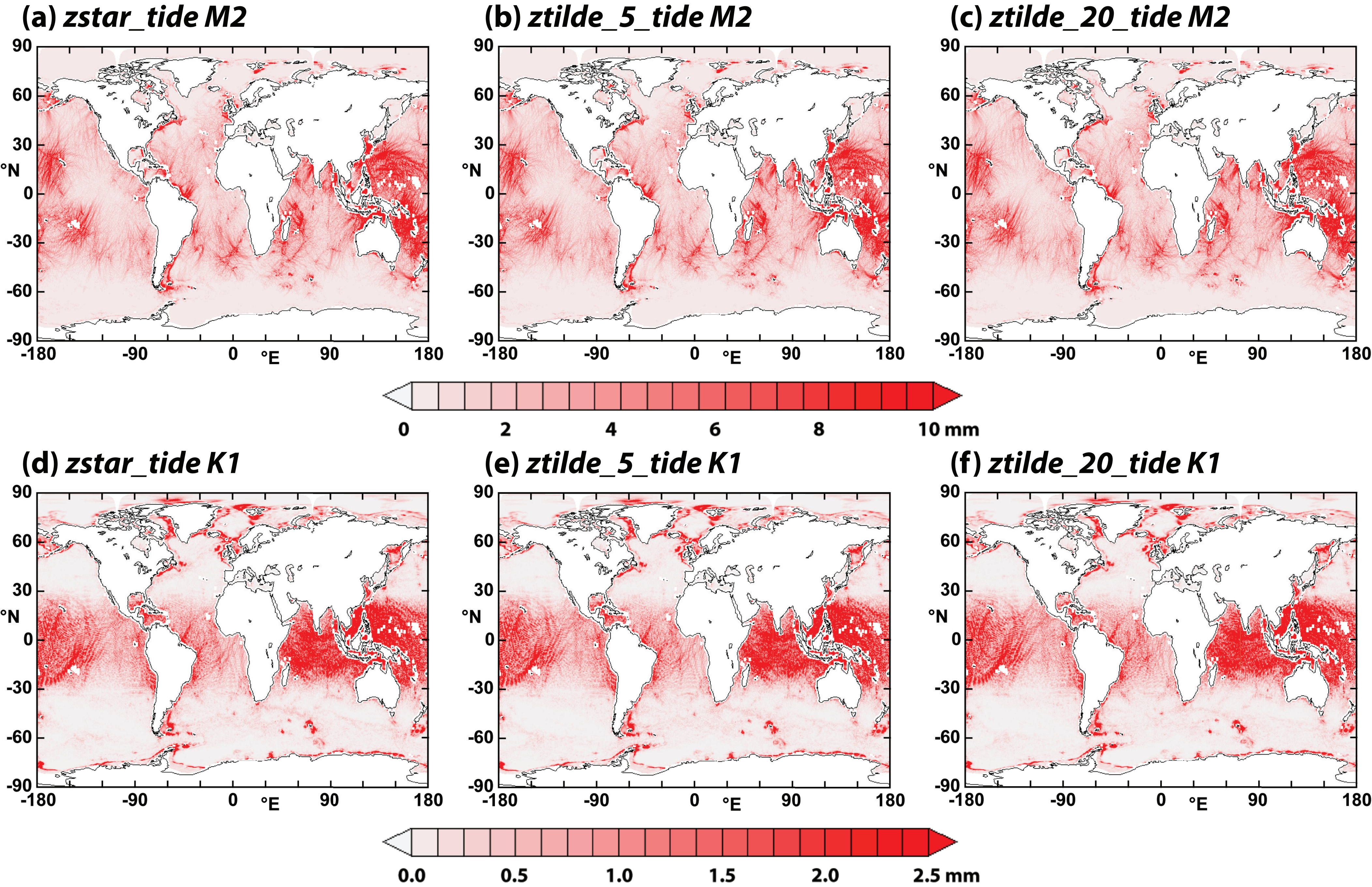

(a) zstar_tide M2
(b) ztilde_5_tide M2
(c) ztilde_20_tide M2
0
2
4
6
8
10 mm
(d) zstar_tide K1
(e) ztilde_5_tide K1
(f) ztilde_20_tide K1
0.0
0.5
1.0
1.5
2.0
2.5 mm
°N
°E
90
60
30
0
-30
-60
-90
-180
-90
0
90
180

Figure 3.

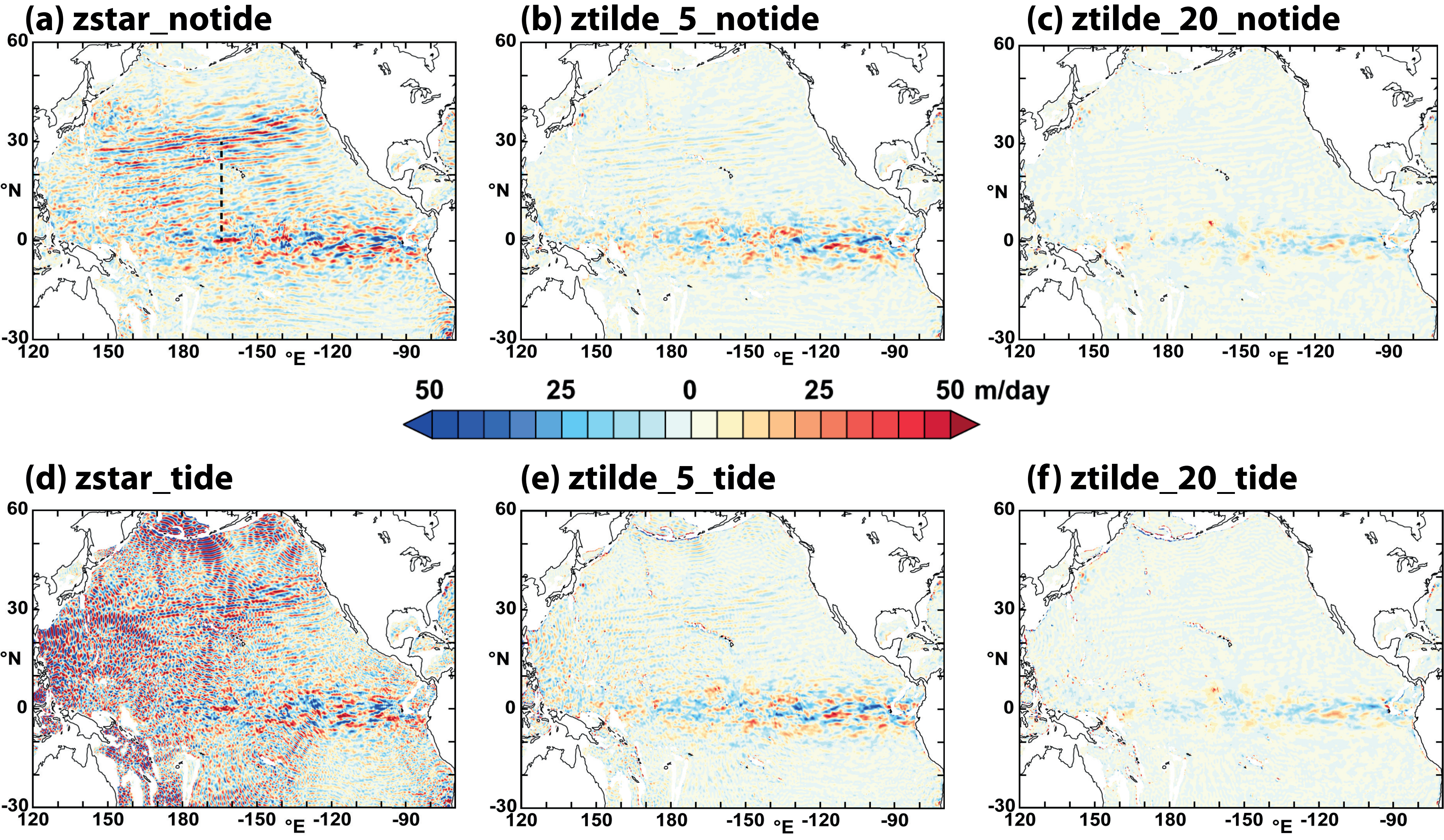

(a) zstar_notide
(b) ztilde_5_notide
(c) ztilde_20_notide
(d) zstar_tide
(e) ztilde_5_tide
(f) ztilde_20_tide
60
30
°N
0
-30
120
150
180
-150
°E
-120
-90
50
25
0
25
50 m/day

Figure 4.

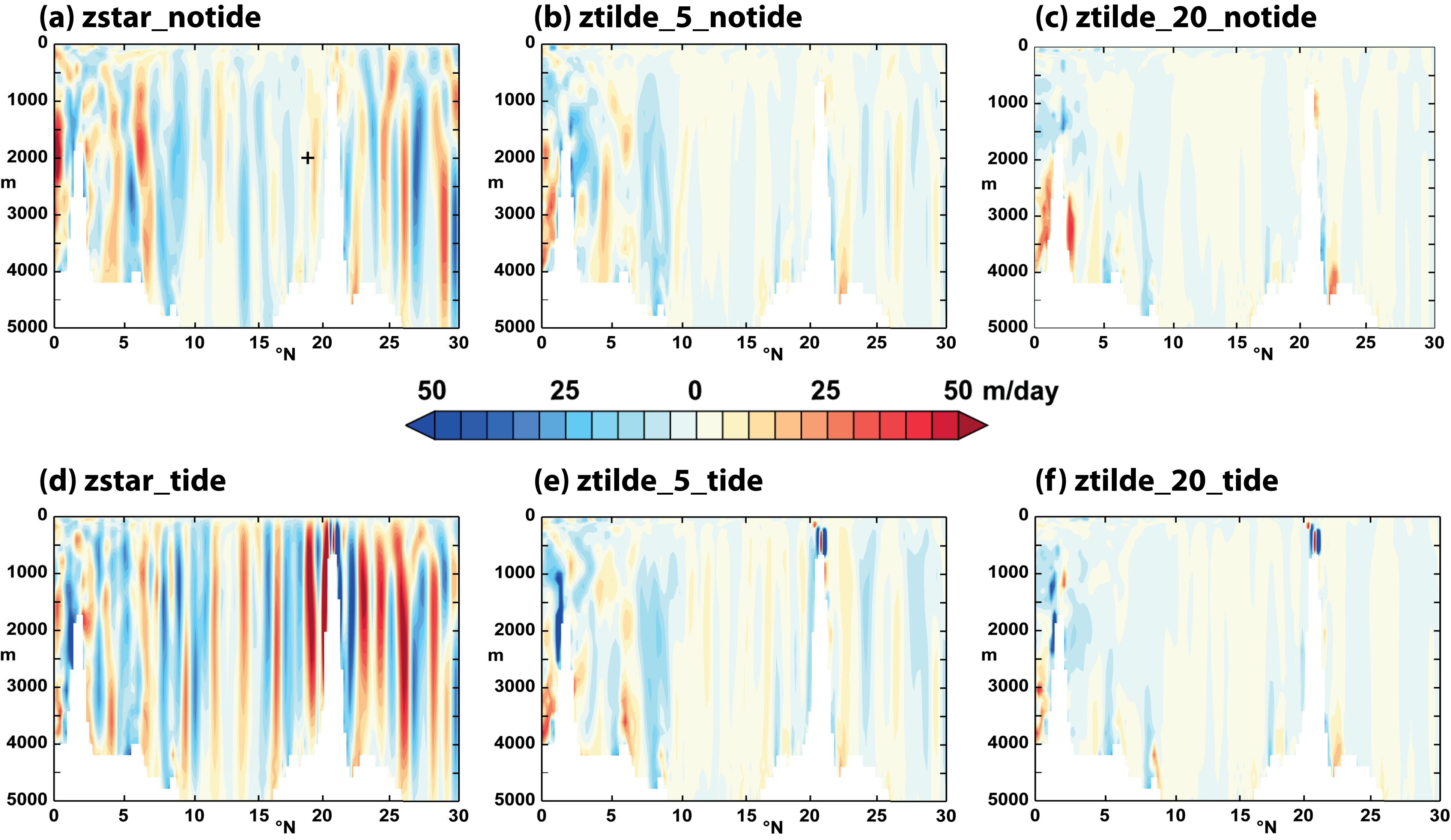
(a) zstar_notide
(b) ztilde_5_notide
(c) ztilde_20_notide
(d) zstar_tide
(e) ztilde_5_tide
(f) ztilde_20_tide
m
°N
0
1000
2000
3000
4000
5000
0
5
10
15
20
25
30
50
25
0
25
50 m/day

Figure 5.

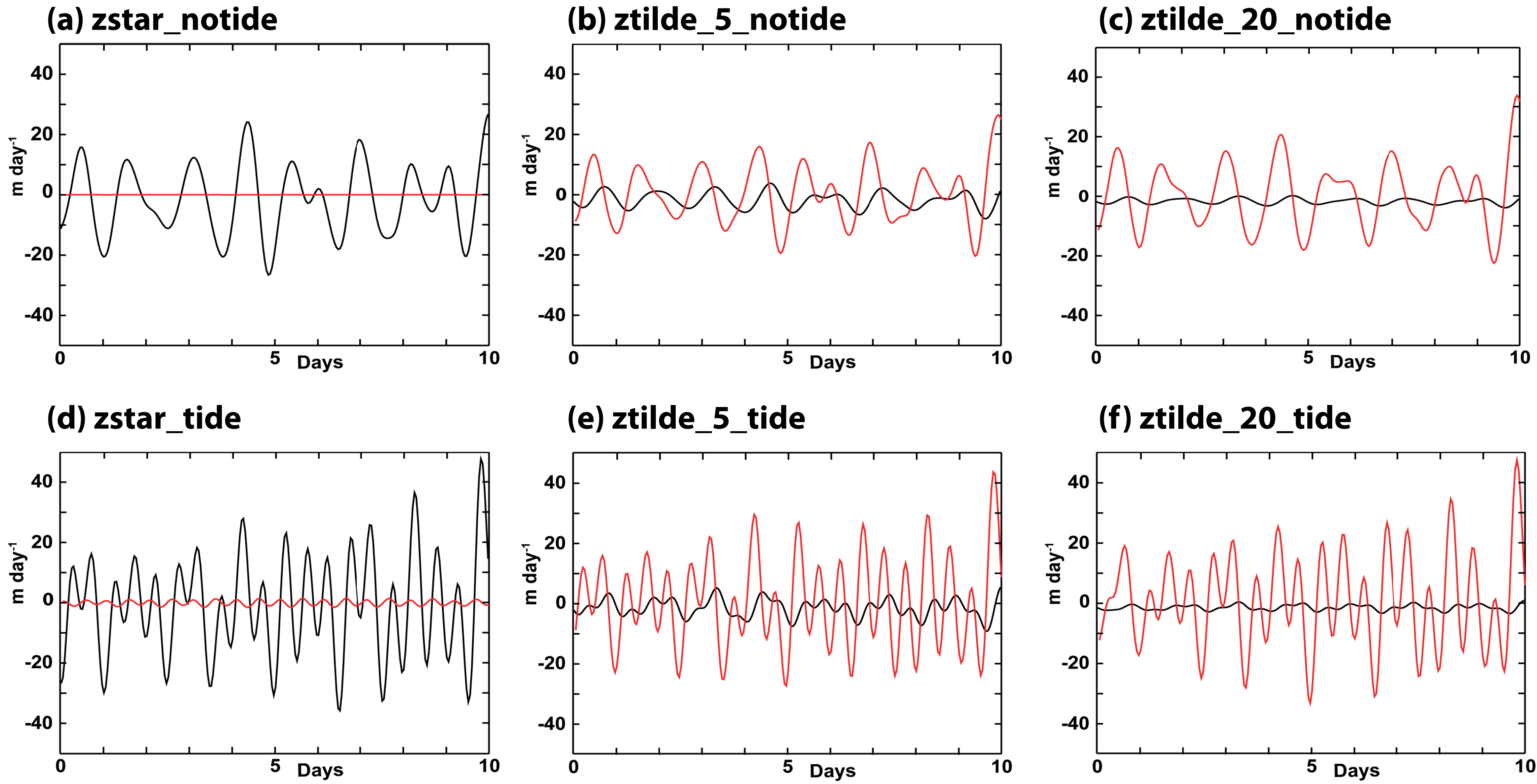

(a) zstar_notide
(b) ztilde_5_notide
(c) ztilde_20_notide
(d) zstar_tide
(e) ztilde_5_tide
(f) ztilde_20_tide
m day-1
Days
40
20
0
-20
-40
0
5
10

Figure 6.

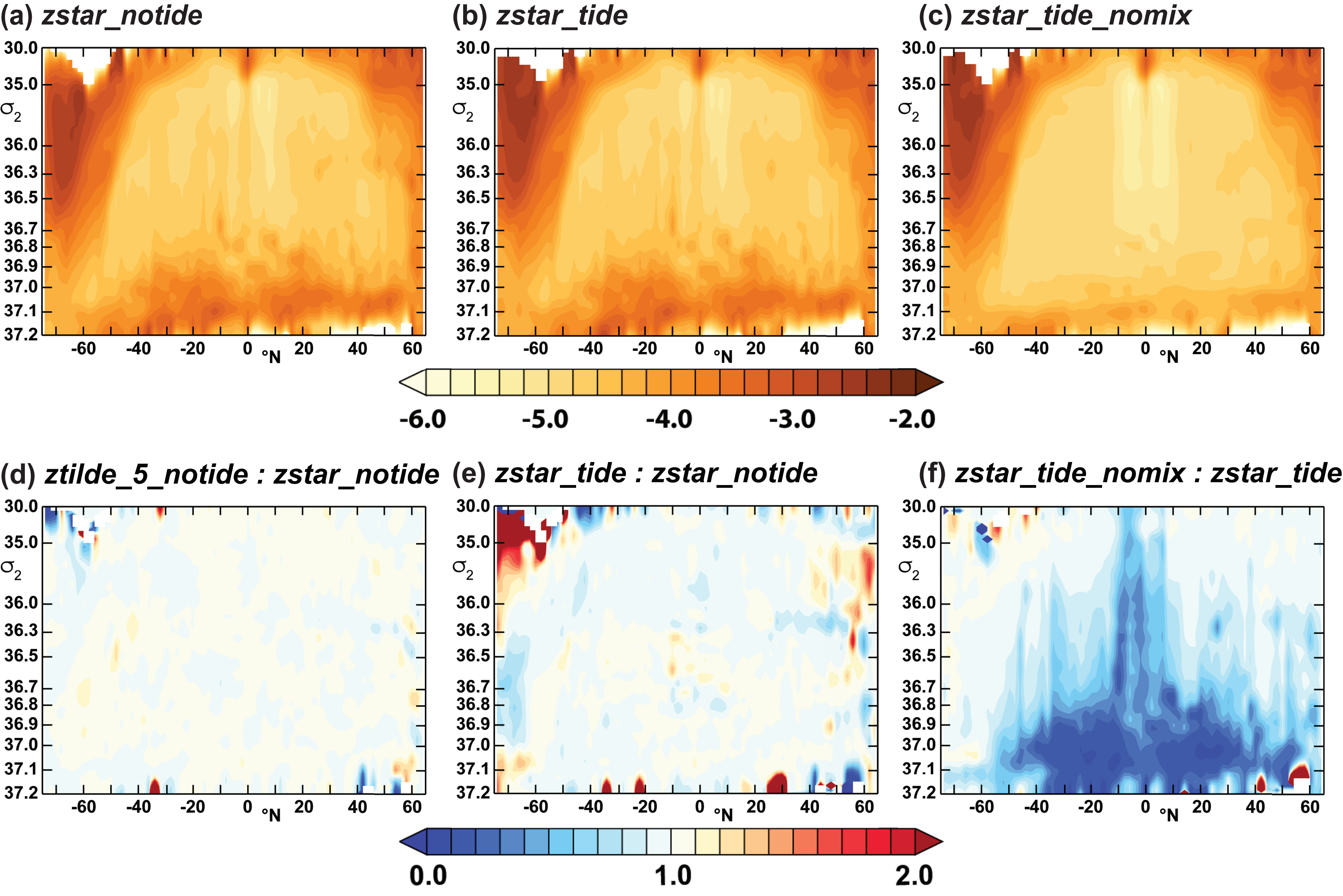

(a) zstar_notide
(b) zstar_tide
(c) zstar_tide_nomix
30.0
35.0
σ2
36.0
36.3
36.5
36.7
36.8
36.9
37.0
37.1
37.2
-60 -40 -20 0 °N 20 40 60
-6.0 -5.0 -4.0 -3.0 -2.0
(d) ztilde_5_notide : zstar_notide
(e) zstar_tide : zstar_notide
(f) zstar_tide_nomix : zstar_tide
0.0 1.0 2.0

Figure 7.

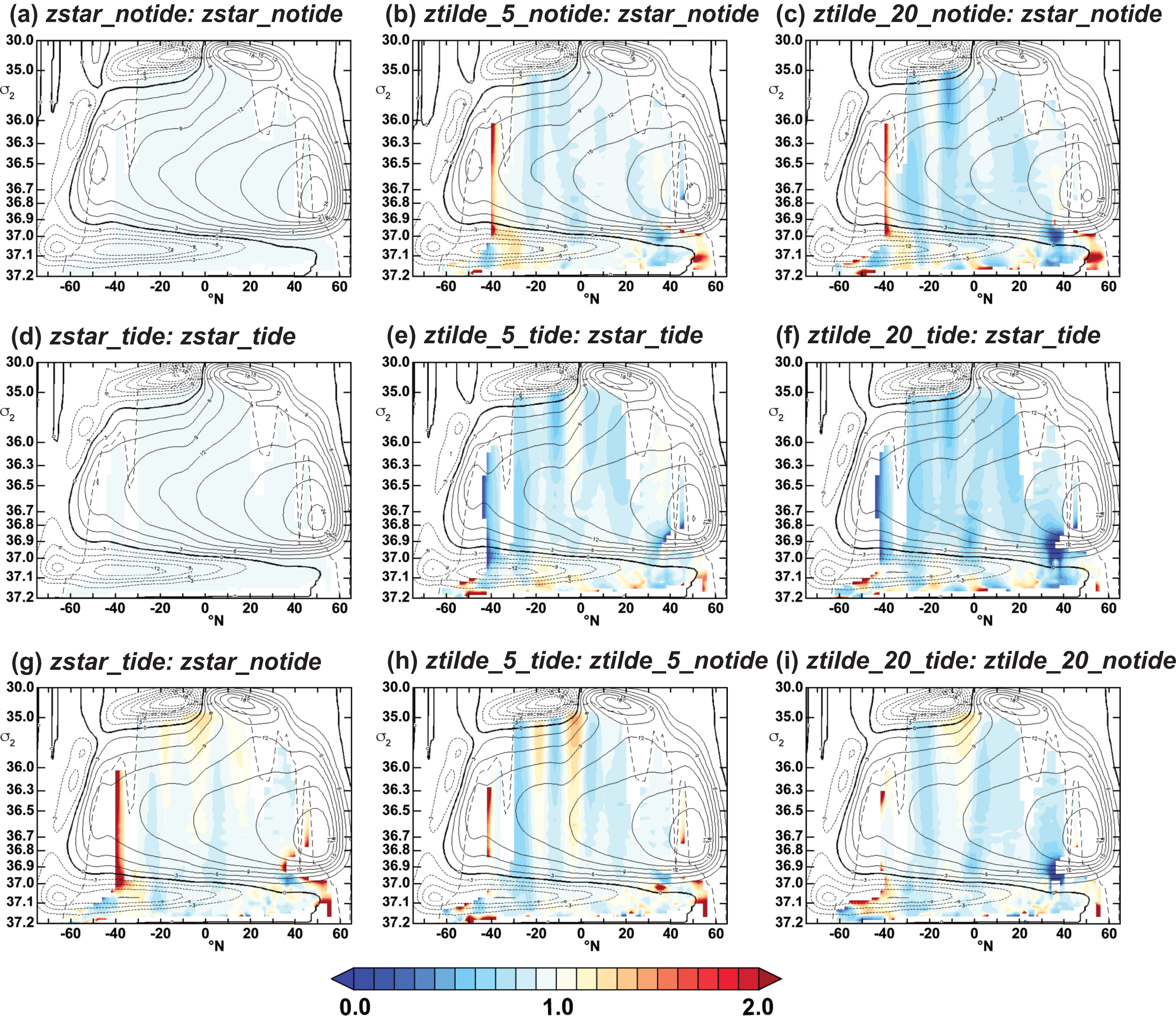

(a) zstar_notide: zstar_notide
(b) ztilde_5_notide: zstar_notide
(c) ztilde_20_notide: zstar_notide
(d) zstar_tide: zstar_tide
(e) ztilde_5_tide: zstar_tide
(f) ztilde_20_tide: zstar_tide
(g) zstar_tide: zstar_notide
(h) ztilde_5_tide: ztilde_5_notide
(i) ztilde_20_tide: ztilde_20_notide
σ2
30.0
35.0
36.0
36.3
36.5
36.7
36.8
36.9
37.0
37.1
37.2
-60
-40
-20
0
20
40
60
°N
0.0
1.0
2.0

Figure 8.

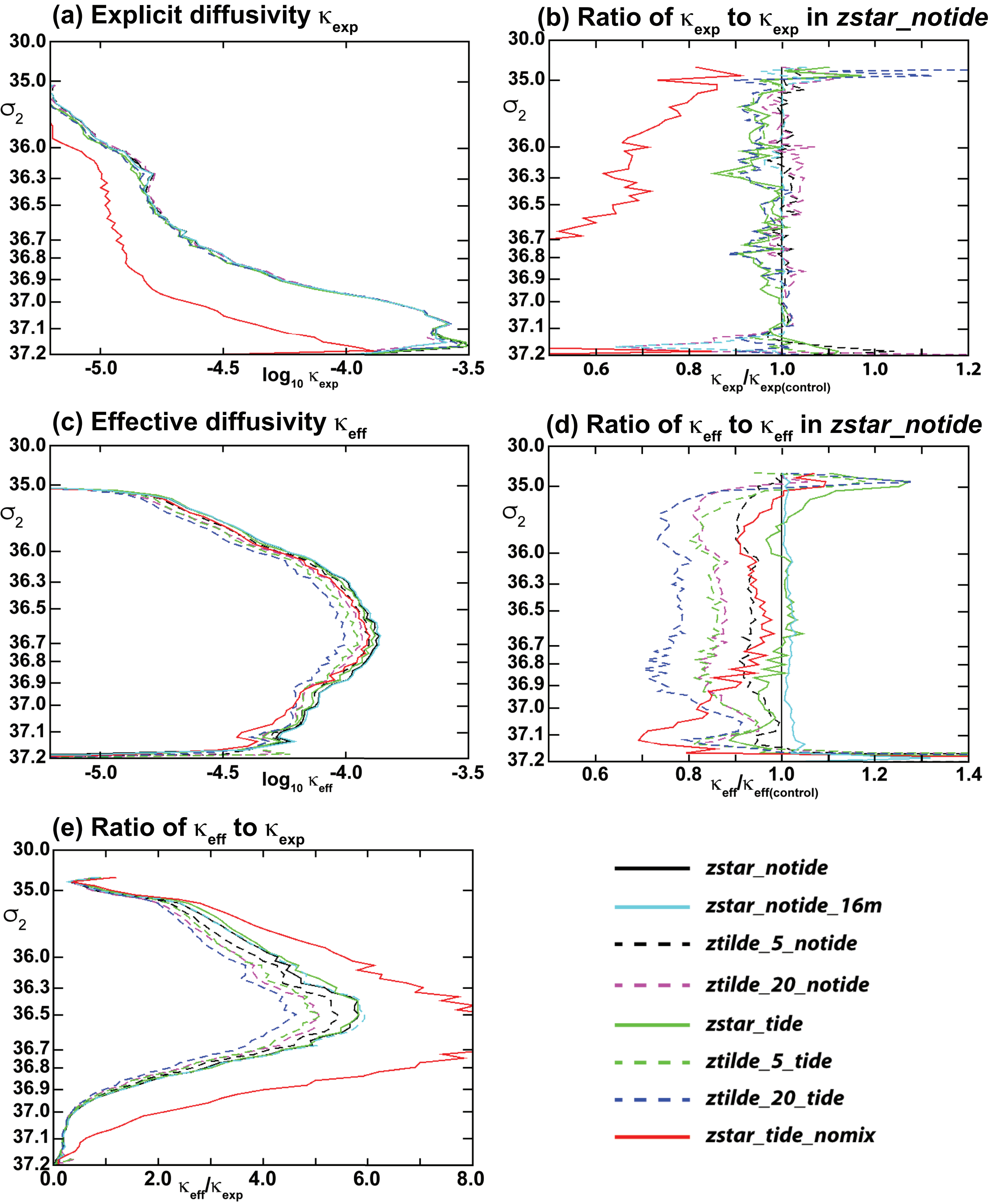

(a) Explicit diffusivity κ_{exp}
σ_2
30.0
35.0
36.0
36.3
36.5
36.7
36.8
36.9
37.0
37.1
37.2
-5.0
-4.5
-4.0
-3.5
$\log_{10} \kappa_{exp}$
(b) Ratio of κ_{exp} to κ_{exp} in *zstar_notide*
0.6
0.8
1.0
1.0
1.2
$\kappa_{exp}/\kappa_{exp(control)}$
(c) Effective diffusivity κ_{eff}
$\log_{10} \kappa_{eff}$
(d) Ratio of κ_{eff} to κ_{eff} in *zstar_notide*
0.6
0.8
1.0
1.2
1.4
$\kappa_{eff}/\kappa_{eff(control)}$
(e) Ratio of κ_{eff} to κ_{exp}
0.0
2.0
4.0
6.0
8.0
$\kappa_{eff}/\kappa_{exp}$
zstar_notide
zstar_notide_16m
ztilde_5_notide
ztilde_20_notide
zstar_tide
ztilde_5_tide
ztilde_20_tide
zstar_tide_nomix

Figure 9.

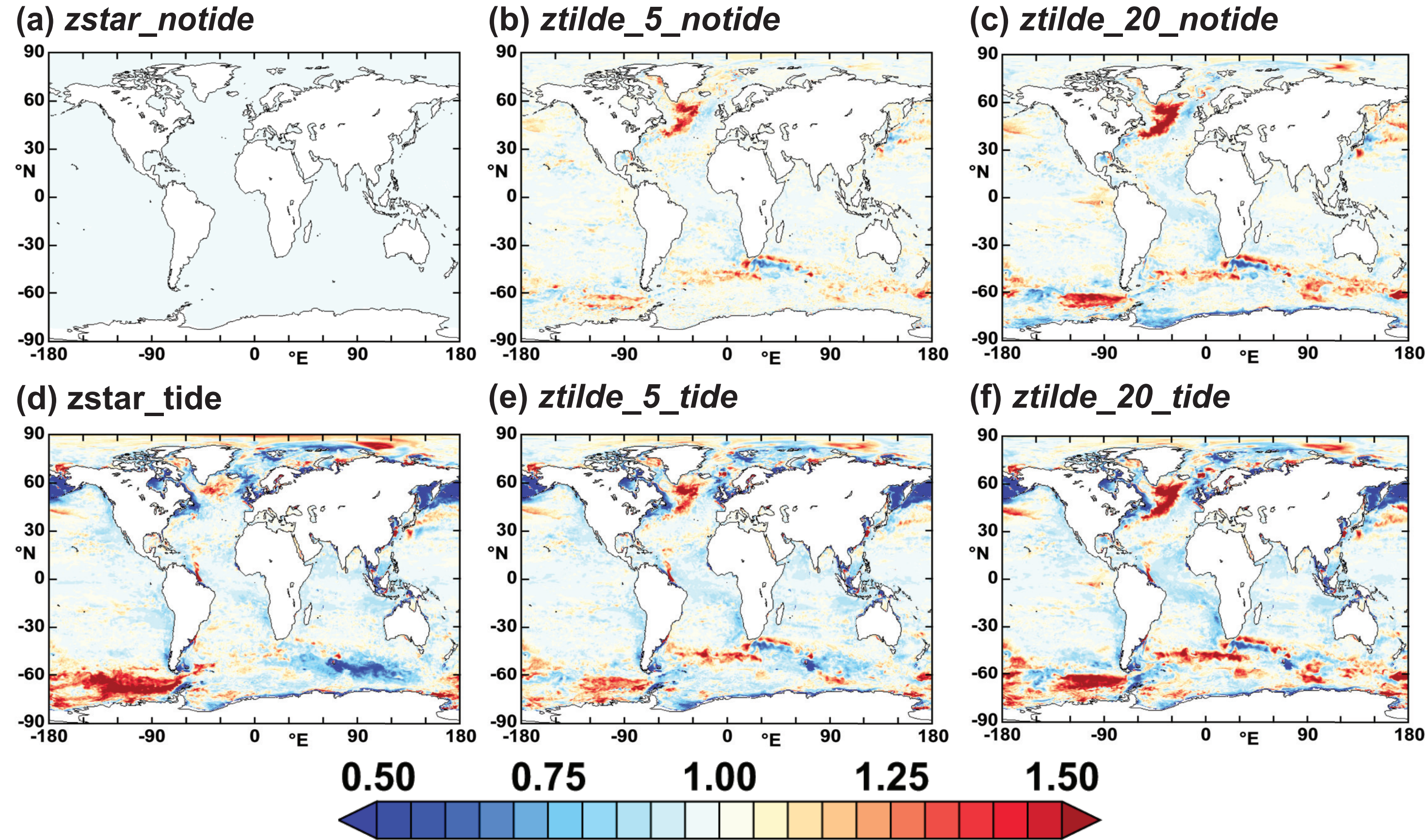

(a) zstar_notide
(b) ztilde_5_notide
(c) ztilde_20_notide
(d) zstar_tide
(e) ztilde_5_tide
(f) ztilde_20_tide
90
60
30
°N
0
-30
-60
-90
-180
-90
0
°E
90
180
0.50
0.75
1.00
1.25
1.50

Figure 10.

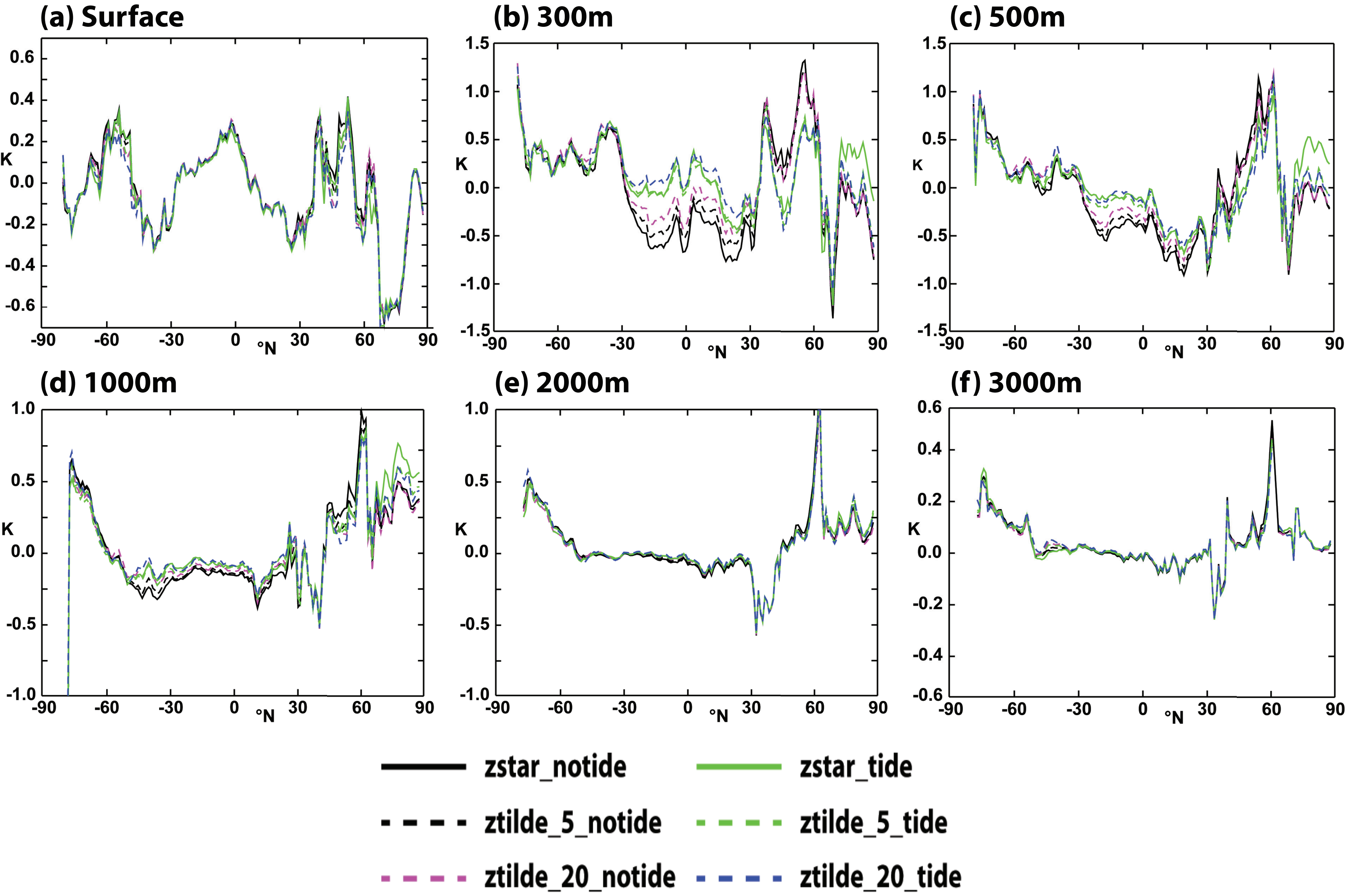

(a) Surface
(b) 300m
(c) 500m
(d) 1000m
(e) 2000m
(f) 3000m
K
°N
zstar_notide
zstar_tide
ztilde_5_notide
ztilde_5_tide
ztilde_20_notide
ztilde_20_tide

Figure 11.

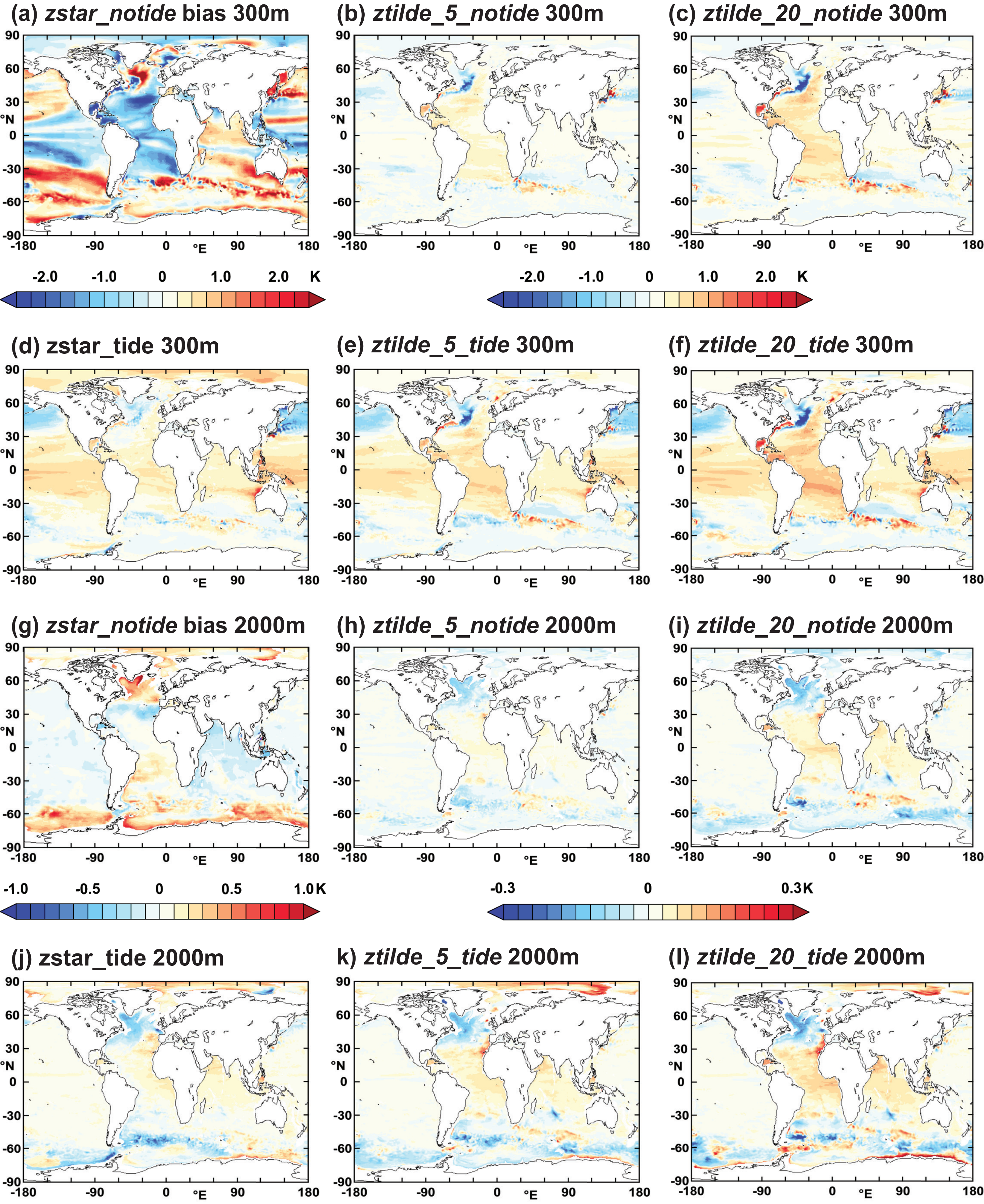
(a) zstar_notide bias 300m
(b) ztilde_5_notide 300m
(c) ztilde_20_notide 300m
-2.0 -1.0 0 1.0 2.0 K
(d) zstar_tide 300m
(e) ztilde_5_tide 300m
(f) ztilde_20_tide 300m
(g) zstar_notide bias 2000m
(h) ztilde_5_notide 2000m
(i) ztilde_20_notide 2000m
-1.0 -0.5 0 0.5 1.0K
-0.3 0 0.3K
(j) zstar_tide 2000m
k) ztilde_5_tide 2000m
(l) ztilde_20_tide 2000m
°N
°E

Figure 12.

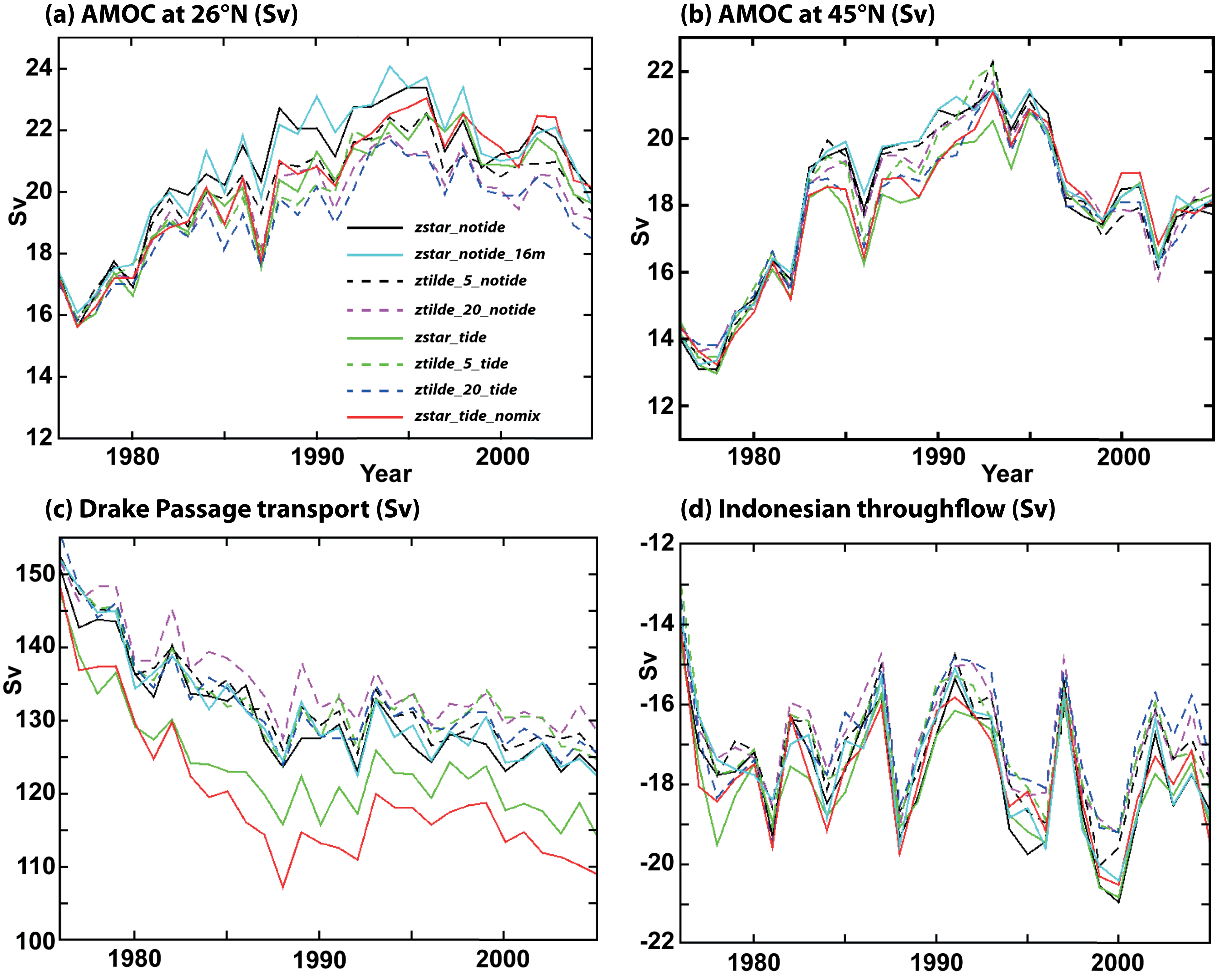

(a) AMOC at 26°N (Sv)
(b) AMOC at 45°N (Sv)
(c) Drake Passage transport (Sv)
(d) Indonesian throughflow (Sv)
Sv
Year
1980
1990
2000
zstar_notide
zstar_notide_16m
ztilde_5_notide
ztilde_20_notide
zstar_tide
ztilde_5_tide
ztilde_20_tide
zstar_tide_nomix

Figure 13.

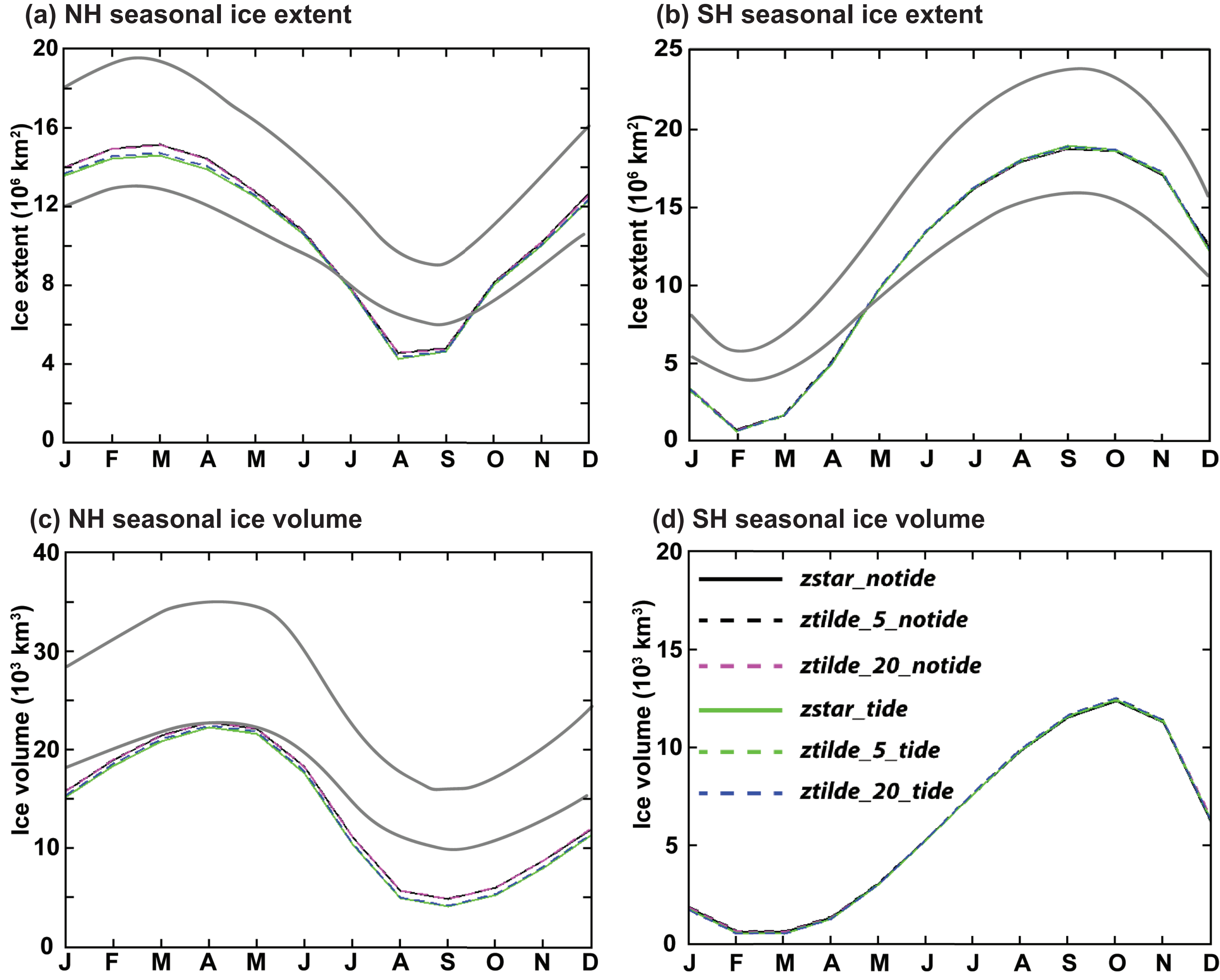
(a) NH seasonal ice extent
(b) SH seasonal ice extent
(c) NH seasonal ice volume
(d) SH seasonal ice volume
Ice extent (10^6 km^2)
Ice volume (10^3 km^3)
J F M A M J J A S O N D
zstar_notide
ztilde_5_notide
ztilde_20_notide
zstar_tide
ztilde_5_tide
ztilde_20_tide